1

2

3

4

5

6

Influence of Stratification and Wind Forcing on the Dynamics of Lagrangian

Residual Velocity in a Periodically Stratified Estuary

Fangjing Deng[1], Feiyu Jia[1], Rui Shi[2], Shuwen Zhang[1], Qiang Lian[1], Xiaolong Zong[1],

Zhaoyun Chen[1,*]

[1] *Guangdong Provincial Key Laboratory of Marine Disaster Prediction and Prevention, Institute of Marine*
Sciences, Shantou University, Shantou, 515063, China

[2] *State Key Laboratory of Tropical Oceanography, South China Sea Institute of Oceanology, Chinese Academy*
of Sciences, Guangzhou, China

15

16

17

Correspondence to: Zhaoyun Chen (chenzy@stu.edu.cn)

19

20

21

1

Abstract

Wind and stratification play pivotal roles in shaping the structure of the Lagrangian residual velocity (LRV). However, the intricate dynamics by which wind and stratification modify the LRV remain poorly studied. This study derives numerical solutions of LRV components and eddy viscosity subcomponents to elucidate the dynamics within the periodically stratified Pearl River estuary. The vertical shear cross-estuary LRV (u_L) is principally governed by the interplay among the eddy viscosity component (u_{Ltu}), the barotropic component (u_{Lba}), and the baroclinic component (u_{Lgr}) under stratified conditions. During neap tides, southwesterly winds notably impact u_L by escalating u_{Ltu} by an order of magnitude within the upper layer. This transforms the eastward flow dominated by u_{Ltu} under wind influence into a westward flow dominated by u_{Lba} in upper shoal regions without wind forcing. The along-estuary LRV exhibits a gravitational circulation characterized by upper-layer outflow engendered by barotropic component (v_{Lba}) and lower-layer inflow predominantly driven by baroclinic component (v_{Lgr}). The presence of southwesterly winds suppresses along-estuary gravitational circulation by diminishing the magnitude of v_{Lba} and v_{Lgr}. The contributions of v_{Lba} and v_{Lgr} are approximately equal, while the ratio between u_{Lba} and u_{Lgr} (u_{Ltu}) fluctuates within the range of 1 to 2 in stratified waters. Under unstratified conditions, LRV exhibits a lateral shear structure due to differing dominant components compared to stratified conditions. In stratified scenarios, the eddy viscosity component of LRV is predominantly governed by the turbulent mean component, while it succumbs to the influence of the tidal straining component in unstratified waters.

1. Introduction

Tidal currents are the principal movement in shallow seas and estuaries. However, tidal oscillations are not the predominant factor regarding the long-term transport of mass, such as pollutants, sediments, nutrients, and suspended materials. Instead, residual current, which remains after filtering out tidal movements, plays a crucial role in long-term mass transport. Therefore, unveiling the dynamic mechanisms governing the structure and magnitude of the residual current becomes particularly important for a correct understanding of the circulation and long-term mass transport in shallow seas and estuaries.

Pritchard (1952) proposed a conceptual model of estuarine circulation characterized by a two-layer structure, drawing from extensive observations. A subsequent study by Pritchard (1956) emphasized the crucial role of the horizontal density gradient as the primary driving force for estuarine circulation. Subsequently, the theory of estuarine gravitational circulation was developed, assuming a constant eddy viscosity (Hansen and Rattray, 1965). Nevertheless, it is imperative to acknowledge that estuarine circulation is influenced not solely by density gradients but also by factors such as wind, tides, and other dynamic forces. These external factors possess the ability to modify or even reverse the structure of gravitational circulation within estuaries.

To remove the tidal signal, early researchers such as Abbott (1960) utilized a straightforward method by averaging current velocities over one or several tidal periods at a specific location to calculate the Eulerian Residual Velocity (ERV). Several studies have highlighted the impact of tidal straining on Eulerian residual velocity (ERV) (e.g., Becherer et al., 2011; Burchard et al., 2014, 2023). Jay and Musiak (1994) found the ERV induced by tidal straining is comparable to gravitational circulation. Additionally, tidal straining contributes twice as much to the ERV as gravitational circulation without consideration of river runoff (Burchard and Hetland, 2010). The flow induced by tidal straining varies in estuaries with

different stratified conditions. When the horizontal density gradient is small, tidal straining dominates the structure of the ERV (Burchard et al., 2011). Cheng et al. (2011) showed that tidal straining induces a typical two-layer circulation in weakly stratified estuaries, while the circulation exhibits a vertical three-layer structure with inflow in the upper and lower layer and outflow in the middle layer in partially and strong stratified estuaries. As stratification intensifies, the ratio of flow induced by tidal straining to gravitational circulation decreases. In a weakly stratified short estuary, tidal straining plays a secondary role in ERV compared to gravitational circulation (Wei et al., 2021). Geyer and MacCready (2014) indicated that the Eulerian mean method tends to overestimate the contribution of tidal straining. Therefore, it is more reasonable to analyze dynamical mechanisms for residual current from the perspective of the Lagrangian tidally averaged theory.

Wind, in conjunction with tides and density gradients, exerts a substantial influence on estuarine residual currents and stratification (Verspecht et al., 2009; Jongbloed et al., 2022). Its role in the generation of surface residual currents is underscored by the strong correlations observed between wind speeds and residual current velocities across both annual and seasonal timescales (Ren et al., 2022). Research on the Dongsha atoll revealed that the combined effects of wind and tide introduce more dynamic water exchange compared to tides alone (Chen, 2023). In the Bohai Sea area off Qinhuangdao, residual currents exhibit pronounced seasonal fluctuations, correlating notably with wind speeds at specific temporal lags (Zhang et al., 2023). Furthermore, the shift in wind-driven circulation is pivotal for mass transport within bays, with estuarine residual circulation superseding tidal pumping as the primary transport mechanism (Young et al., 2023). Burchard (2009) highlighted that upstream winds weaken stratification and reduce the magnitude of the ERV, whereas the downstream wind sheds the opposite effect. To quantify the destratification effect of upstream wind, Lange and Burchard (2019) introduced the Wedderburn number to analyze the relationship between upstream wind and density

94   gradient. The wind is less inclined to affect the residual current with large Wedderburn numbers

95   and may inhibit gravitational circulation, whereas the structure of ERV reverses with small

96   Wedderburn numbers. Wind plays a pivotal role in modulating classical gravitational

97   circulation, most notably reversing surface outflow during winter. In contrast, northward winds

98   in spring enhance stratification and augment the pressure gradient-driven flow (Soto-Riquelme

99   et al., 2023).

100   The Eulerian mean method is a prevalent approach for examining estuarine dynamics;

101   however, specific terms within its momentum and mass transport equations remain ambiguous

102   in their physical interpretations (Ianniello, 1977; Feng et al., 1984). Lamb (1975) posited that

103   any flow field must adhere to the mass conservation principle. Zimmerman (1979) defined

104   Lagrangian residual velocity (LRV) as the net displacement of the water parcels over one or

105   several tidal periods. Contextualizing this, the LRV, rooted in the intrinsic principles of physical

106   motion, upholds material conservation, and offers a precise portrayal of circulation dynamics

107   in shallow marine environments (Feng, 1987; Jiang and Feng, 2014).

108   Lagrangian particle tracking methods play a pivotal role in studying mass transport and

109   residence time (RT) across various coastal seas, estuaries, and bays. Specific water mass

110   transport patterns are discerned in the Bohai Sea, revealing salient regional transport

111   characteristics steered by LRV (Yu et al., 2023). The combined effects of residual transport

112   velocity in the current and next seasons emerge as the predominant factor driving the RT's

113   seasonal variation (Lin et al, 2022). Wind direction, wind speed, and density gradient-induced

114   circulation collectively regulate RT (Hewageegana et al., 2023). The reduction of cross-shore

115   currents results in mass convergence and increases RT (Li et al., 2022). The water exchange

116   and RT are mainly determined by the structure of the LRV (Jiang and Feng, 2014). RT

117   predominantly represents an accumulative measure, primarily influenced by residual transport

118   rather than immediate responses (Jiang, 2023). Convergence zones resulting from LRV

119 efficiently establish consistent aggregation regions of buoyant material within the estuary

120 rather than ERV (Kukulka and Chant, 2023). To gain an in-depth understanding of mass

121 transport, extensive prior research has been dedicated to elucidating qualitative and quantitative

122 evaluations of the determinants impacting the LRV's structure and magnitude. The influence of

123 LRV in semi-closed estuaries and bays affected by tides has received attention from

124 oceanographers (Winant, 2008; Jiang and Feng, 2011; Deng et al., 2019). Quan et al. (2014)

125 employed a numerical model to investigate the impact of the ratio of tidal amplitude to water

126 depth on LRV, and Jiang and Feng (2014) explored how the ratio of estuary length to

127 wavelength affects LRV. Wang et al. (2010) examined the effects of wind, density gradient, and

128 river runoff on LRV using a numerical model. However, this study aims to illustrate structural

129 and magnitudinal variations of the total LRV under different factors, without delving into the

130 underlying dynamic mechanisms. Liu et al. (2021) demonstrated that the influence of wind and

131 density gradients on LRV is closely associated with the initial tidal phase based on the

132 momentum equations, but the specific contribution of each dynamic component to LRV

133 remains poorly studied.

134   Jiang and Feng (2014) explored the dynamical mechanisms for the LRV, which gives to

135 the assumptions of a constant eddy viscosity and linear bottom friction in the entire estuarine.

136 Subsequently, numerical models were utilized to study the contribution of tidal body force to

137 LRV under a constant eddy viscosity, revealing that the Stokes' drift component plays a

138 dominant role (Cui et al., 2019). Chen et al. (2020) analyzed the contribution of each dynamical

139 term to the LRV and found the Stokes' drift component is the dominant component under the

140 condition of the horizontal unvaried but depth-varying eddy viscosity. The above studies are

141 all carried out under a temporally constant eddy viscosity. The impact of spatially varying eddy

142 viscosity on LRV was examined in a narrow model, revealing that nonlinearity leads to a more

143 complex LRV structure (Deng et al., 2017). However, these studies lack a quantitative analysis

144   of the underlying dynamical mechanism. Sheng et al. (2022) demonstrated that the structure of

145   LRV is primarily determined by the combined effects of the barotropic pressure gradient and

146   tidal body force when only barotropic conditions are considered. Deng et al. (2022) further

147   quantitatively analyzed the contributions of each driving force to LRV, considering both

148   temporal and spatial variations in eddy viscosity under a constant density gradient. However,

149   the roles of wind and stratification in LRV dynamics remain poorly studied.

150   The Pearl River, as the third largest river in China, encompasses a complex hydrodynamic

151   environment. The Pearl River estuary (PRE) is a trumpet-like estuary characterized by two

152   deep channels and shallow shoals. In recent years, researchers have increasingly focused on

153   topics such as tidal currents, salinity intrusion, river plume dynamics, and residual current in

154   the PRE (e.g., Gong et al., 2018; Pan et al., 2020; Wei et al., 2022). The estuary displays a

155   typical two-layer circulation as observed in micro-tidal estuaries (Xue et al., 2001). Wang (2014)

156   investigated the temporal and spatial variations of the ERV and analyzed its underlying

157   dynamical mechanisms within the PRE. Lai et al. (2018) discussed the influence of tides and

158   winds on the ERV and the associated dynamical processes using the Eulerian mean momentum

159   equation. Additionally, the nonlinear advection term was identified as an important factor in

160   the ERV within the PRE (Xu et al., 2021). An anticlockwise shift in summertime wind direction

161   from 1979 to 2020 weakens cross-channel wind-driven transport and along-channel seaward

162   flow, leading to increased stratification near the Modaomen (Hong et al. 2022). While Chu et

163   al. (2022) explored the hydrodynamic processes and connectivity of the circulation within the

164   estuary from a Lagrangian tidally averaged perspective, a detailed dynamical analysis was not

165   provided. Few studies have focused on the LRV within the PRE, especially regarding its

166   underlying dynamical mechanisms.

167   Analytical solutions regarding the dynamics of LRV are constrained to a temporally

168   constant eddy viscosity, while numerical solutions of LRV's dynamic components disregard

7

169   the influence of stratification and wind. Consequently, the impact of wind and stratification on

170   LRV dynamics remains enigmatic. Numerical solutions for LRV components are derived to

171   grasp the modifications induced by wind and stratification within each LRV component,

172   ultimately leading to changes in the overall LRV. Furthermore, wind and stratification influence

173   turbulent mixing, subsequently affecting the LRV driven by the eddy viscosity term. Although

174   scholars have extensively examined tidal straining effects on estuarine circulation via the

175   Eulerian mean theory, the analysis of turbulent influences from the Lagrangian mean theory

176   perspective yields distinctions from the Eulerian approach. To illuminate the mechanisms

177   underlying the eddy viscosity component of LRV, we initiate by decomposing this component

178   into four subcomponents. This study pursues two principal objectives: 1) to delve into the

179   mechanisms by which wind and stratification modify LRV components, and 2) to investigate

180   the roles of wind and stratification in the dominant contributor of the eddy viscosity component.

181   This paper will provide valuable insights into the dynamic processes of longitudinal and lateral

182   estuarine circulation based on Lagrangian mean theory under the influence of wind and

183   stratification. These aspects have not been quantitatively assessed in previous studies.

184   Additionally, the proposed decomposition theory of the eddy viscosity component offers a

185   novel approach for analyzing the dominant mechanisms of turbulent components. This paper

186   is structured as follows: Section 2 provides a delineation of model setup parameters, model

187   validation, and LRV decomposition methods. Section 3 outlines the contribution of each

188   component to the overall LRV and the contribution of each subcomponent to the total eddy

189   viscosity component of LRV. The discussion and conclusions are presented in Section 4.

190   **2. Theory and model description**

191   **2.1 The decomposition method**

192   The LRV is decomposed into seven components, including the local acceleration

component (u_{Lac} and v_{Lac}), horizontal nonlinear advection component (u_{Ladh} and v_{Ladh}), vertical nonlinear advection component (u_{Ladv} and v_{Ladv}), barotropic pressure gradient component (barotropic component; u_{Lba} and v_{Lba}), baroclinic pressure gradient component (baroclinic component; u_{Lgr} and v_{Lgr}), eddy viscosity component (u_{Ltu} and v_{Ltu}), and horizontal diffusion component (u_{Lho} and v_{Lho}). The detailed decomposition methods are shown in the appendix. Deng et al. (2022) considered a temporally constant density gradient but neglected the effects of periodic stratification and wind forcing. In this paper, one of the primary objectives is to quantify the effects of wind and stratification on the dynamics of the different components of LRV.

Wind and stratification play roles in turbulent mixing, which subsequently impacts the fluctuations of eddy viscosity over a tidal period. This influence extends to the eddy viscosity component of LRV. To clarify the mechanisms underlying this eddy viscosity component, we decompose it into four subcomponents. We evaluate the distinct contributions of each subcomponent to the total eddy viscosity component, aiming to delve into the dominant dynamic mechanisms, which is another objective of our paper. The study derives the following decomposition methods:

$$-\left\langle \frac{1}{D^2}\frac{\partial}{\partial\sigma}\left(v_h\frac{\partial u}{\partial\sigma}\right)\right\rangle/f = -\left\langle \frac{1}{D^2}\frac{\partial}{\partial\sigma}\left(v_{h0}\frac{\partial u_0}{\partial\sigma}\right)\right\rangle/f - \left\langle \frac{1}{D^2}\frac{\partial}{\partial\sigma}\left(v_{h0}\frac{\partial u_1}{\partial\sigma}\right)\right\rangle/f$$
$$-\left\langle \frac{1}{D^2}\frac{\partial}{\partial\sigma}\left(v_{h1}\frac{\partial u_0}{\partial\sigma}\right)\right\rangle/f - \left\langle \frac{1}{D^2}\frac{\partial}{\partial\sigma}\left(v_{h1}\frac{\partial u_1}{\partial\sigma}\right)\right\rangle/f, \tag{1}$$

$$\left\langle \frac{1}{D^2}\frac{\partial}{\partial\sigma}\left(v_h\frac{\partial v}{\partial\sigma}\right)\right\rangle/f = \left\langle \frac{1}{D^2}\frac{\partial}{\partial\sigma}\left(v_{h0}\frac{\partial v_0}{\partial\sigma}\right)\right\rangle/f + \left\langle \frac{1}{D^2}\frac{\partial}{\partial\sigma}\left(v_{h0}\frac{\partial v_1}{\partial\sigma}\right)\right\rangle/f +$$
$$\left\langle \frac{1}{D^2}\frac{\partial}{\partial\sigma}\left(v_{h1}\frac{\partial v_0}{\partial\sigma}\right)\right\rangle/f + \left\langle \frac{1}{D^2}\frac{\partial}{\partial\sigma}\left(v_{h1}\frac{\partial v_1}{\partial\sigma}\right)\right\rangle/f, \tag{2}$$

$$\text{and } u = u_0 + u_1, \ v = v_0 + v_1, \ v_h = v_{h0} + v_{h1}, \tag{3}$$

where <> represents the Lagrangian-averaged operator, u and v are horizontal tidal currents, v_h is the eddy viscosity, u_1 and v_1 are tidal average currents, u_0 and v_0 are tidal periodic oscillation

211   currents, which are referred to as the zero-order terms. These zero-order terms are equivalent

212   in meaning to u' and v' as defined in prior studies (Burchard and Hetland, 2010; Burchard et

213   al., 2011, 2014; Cheng, 2014). The terms u_1 and v_1 correspond to the first-order terms and

214   represent the tidal average current. The v_{h0} is tidal average eddy viscosity, as the zero-order

215   term with v_{h1} representing the tidal periodic oscillation of the eddy viscosity as the first-order

216   term. The D is time-varying depth, σ is sigma coordinate, and f is Coriolis parameter.

217   Employing a first-order Taylor expansion, the approximation of $1/D^2$ is represented as $1/H^2 -$

218    $2\zeta/H^3$ (Cheng, 2014), where H signifies the mean depth and ζ corresponds to the sea surface

219   elevation. Within the vast majority of the Pearl River Estuary, the ratio of ζ_{max} to H remains

220   below 0.2 during neap tides, with an exception in nearshore areas, where ζ_{max} is the maximum

221   of tidal elevations during a tidal period. The ratio during spring tides is slightly larger than that

222   during neap tides. But whether during spring or neap tides, the terms associated with $1/H^2$

223   exhibit a close correspondence to those related to $1/D^2$ in Eqs. (1) and (2) (not shown). The

224   terms pertaining to $-2\zeta/H^3$ are sufficiently minor to be negligible. Consequently, considering

225   D is approximately equivalent to H, further decomposition of D in the manuscript is not

226   undertaken. The $-\langle\frac{1}{D^2}\frac{\partial}{\partial\sigma}\left(v_{h0}\frac{\partial u_0}{\partial\sigma}\right)\rangle/f$ and $\langle\frac{1}{D^2}\frac{\partial}{\partial\sigma}\left(v_{h0}\frac{\partial v_0}{\partial\sigma}\right)\rangle/f$ represent the coupled

227   component of the tidal-average eddy viscosity and velocity gradient oscillation (v_{Lk0u0} and

228   u_{Lk0u0}), the $-\langle\frac{1}{D^2}\frac{\partial}{\partial\sigma}\left(v_{h1}\frac{\partial u_0}{\partial\sigma}\right)\rangle/f$ and $\langle\frac{1}{D^2}\frac{\partial}{\partial\sigma}\left(v_{h1}\frac{\partial v_0}{\partial\sigma}\right)\rangle/f$ represent the tidal straining

229   component (v_{Lk1u0} and u_{Lk1u0}), the $-\langle\frac{1}{D^2}\frac{\partial}{\partial\sigma}\left(v_{h0}\frac{\partial u_1}{\partial\sigma}\right)\rangle/f$ and $\langle\frac{1}{D^2}\frac{\partial}{\partial\sigma}\left(v_{h0}\frac{\partial v_1}{\partial\sigma}\right)\rangle/f$ represent the

230   turbulent mean component (v_{Lk0u1} and u_{Lk0u1}), the $-\langle\frac{1}{D^2}\frac{\partial}{\partial\sigma}\left(v_{h1}\frac{\partial u_1}{\partial\sigma}\right)\rangle/f$ and $\langle\frac{1}{D^2}\frac{\partial}{\partial\sigma}\left(v_{h1}\frac{\partial v_1}{\partial\sigma}\right)\rangle/$

231   f represent the coupled component of eddy viscosity oscillation and the tidal-average velocity

232   gradient (v_{Lk1u1} and u_{Lk1u1}).

233   **2.2 Model configuration and experiments**

234   This study employs the Finite Volume Coastal Ocean Model (FVCOM; Chen et al., 2006)

235   to simulate the dynamic response of LRV to wind and stratification in the PRE. FVCOM is a

236   three-dimensional primitive equation Community Ocean Model (Chen et al., 2003) that utilizes

237   a finite-volume approach, accounting for a free-surface and employing prognostic techniques.

238   The model consists of unstructured triangular cells and employs terrain-following vertical

239   coordinates, allowing for a better fitness of the irregular coastline and complex topography

240   present in the estuary.

241   The model domain, covering the PRE and adjacent coastal regions, is depicted in Fig. 1,

242   spanning from 111.5°E to 116.5°E and 20°N to 23°N. The open boundary is situated in the

243   northern South China Sea. Unidirectional grid nesting is implemented to enhance solution

244   algorithms. The coarse grid consists of 8040 nodes and 15093 triangular elements. The spatial

245   resolution of the horizontal grids varies across the entire region, ranging from 1 to 10 km.

246   Specifically, a resolution of 1 km is employed within the PRE, 2.0–5.0 km off the Guangdong

247   coast, and 10 km near the open boundary (Fig. 1a). On the other hand, the fine grid, consisting

248   of 45,368 nodes and 87,179 triangular elements, is configured based on the settings from

249   previous studies (e.g., Lai et al., 2018; Geyer et al., 2020; Xu et al., 2021). The spatial resolution

250   of the fine grids within the region also varies, ranging from 0.1 to 2.0 km. More specifically, a

251   resolution of 0.1 km is utilized within the PRE, 0.1–1.0 km off the Guangdong coast, and 2.0

252   km close to the open boundary (Fig. 1b). In the vertical direction, the model employs fourteen

253   uniformly assigned sigma levels.
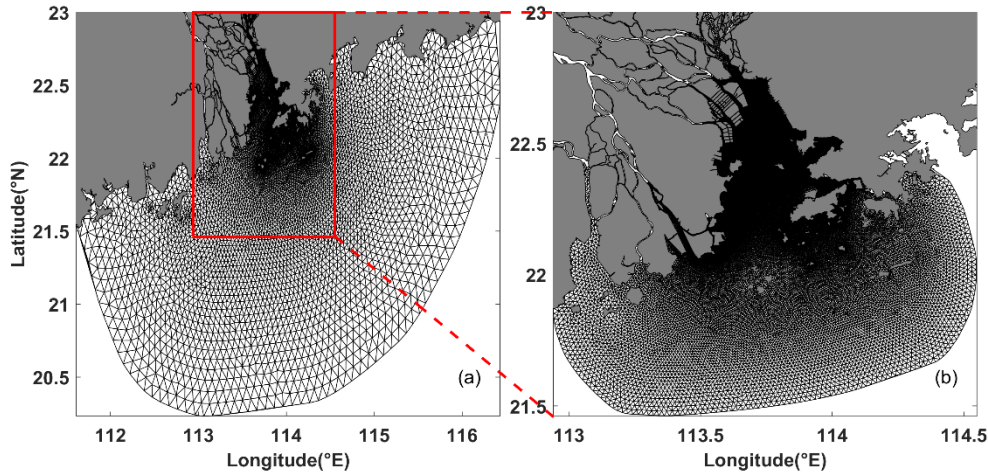
Figure 1 (a) Coarse mesh model, **(b)** fine mesh model.

The model incorporates eight major tidal constituents, namely M_2, N_2, S_2, K_2, K_1, O_1, P_1, and Q_1, as tidal driving forces at the open boundary. These constituents are obtained from the Oregon State University Tidal Prediction Software (OTPS/TPXO; https://www.tpxo.net/otps; Egbert and Svetlana, 2002). To initialize the model, salinity climatological data from the 1° World Ocean Atlas 2009 (WOA2009) dataset is utilized (https://accession.nodc.noaa.gov/0094866; Levitus, 2013). The wind data used in this study are obtained from the monthly averaged Cross-Calibrated Multi-Platform (CCMP) dataset, which has spatial resolutions of 0.25×0.25 degrees (http://www.remss.com/measurements/ccmp; Mears et al., 2022). The Pearl River Estuary (PRE) experiences seasonal reversing monsoonal winds, as documented by Pan et al. (2014) and Pan and Gu (2016). The monthly-averaged CCMP wind data indicate prevalent southwesterly winds during the summer season. Our investigation specifically focuses on the impact of southwesterly winds on the dynamics of Lagrangian Residual Velocity (LRV). The lateral boundary incorporates monthly average river runoff data from eight river inlets, which are provided by the Water Conservancy Committee of the Pearl River under the Ministry of Water Resources. The topography data off the PRE is from the ETOPO2 dataset of NOAA (https://www.ngdc.noaa.gov/mgg/global/relief/ETOPO2/-

272　ETOPO2v2-2006/; NOAA National Geophysical Data Center, 2006), while the topography

273　within the estuary is derived from electronic nautical chart data provided by the China Maritime

274　Safety Administration.

275　　　The coarse grid model simulates a period from 1 January to 31 August 2017, and it reaches

276　a quasi-steady state after one month. In this study, the outputs from the coarse grid model are

277　utilized as the initial and boundary conditions for the fine grid model. The fine grid model,

278　which begins on 1 June 2017, stabilizes after one month. The analysis focuses on the results

279　from the fine grid model obtained on 24 July 2017 during spring tides and 2 August 2017 during

280　neap tides. A split-mode time stepping method is employed with 2-second external and 10-

281　second internal time steps for the coarse grid model, respectively. The fine grid model uses a

282　0.5-second external time step, which is half of the time step used in the coarse grid model. The

283　bottom friction in the model is based on the quadratic bottom friction law, and the calculation

284　of the eddy viscosity coefficient employs the Mellor-Yamada 2.5 order turbulent closure model.

285　　　To investigate the effects of wind and stratification on the dynamics of LRV, Case 1

286　(reference case) includes wind forcing and periodic stratification. Case 2 examines the

287　influence of wind by removing wind forcing compared to Case 1. Case 3 explores the effects

288　of stratification by imposing a uniformly constant salinity and temperature without considering

289　river discharge compared to Case 2 (Table 1). The constant salinity and temperature, with

290　values of 28 °C and 32 psu, respectively, are derived by averaging WOA2009 data for July and

291　August across the whole domain.

Table 1 Numerical experiment scenarios

Experiments	Wind	Tide	Stratification
Case 1 (Reference case)	√	√	√
Case 2	×	√	√
Case 3	×	√	×

292　**2.3 Model verification**

293   The PRE is oriented in the north-south direction (Fig. 2). Accordingly, the positive x-axis,

294   u, and u_L direct eastward; the positive y-axis, v, and v_L direct northward; and the positive z-axis,

295   w, and w_L direct upward. In this context, u and v correspond to the cross-estuary and along-

296   estuary velocities, respectively, with u_L and v_L denoting the corresponding LRV. The paper

297   selects four sections, including three cross sections (Sections B–D) and one along-estuary

298   section (Section A), which roughly cover the PRE (black lines in Fig. 2a). The examination of

299   LRV components and the eddy viscosity subcomponent is presented solely in Section C, given

300   the uniform conclusions derived across four sections. Moreover, the chosen cross-section,

301   Section C, aptly depicts the differential dynamics of LRV between the shoal and the deep

302   channel.

303
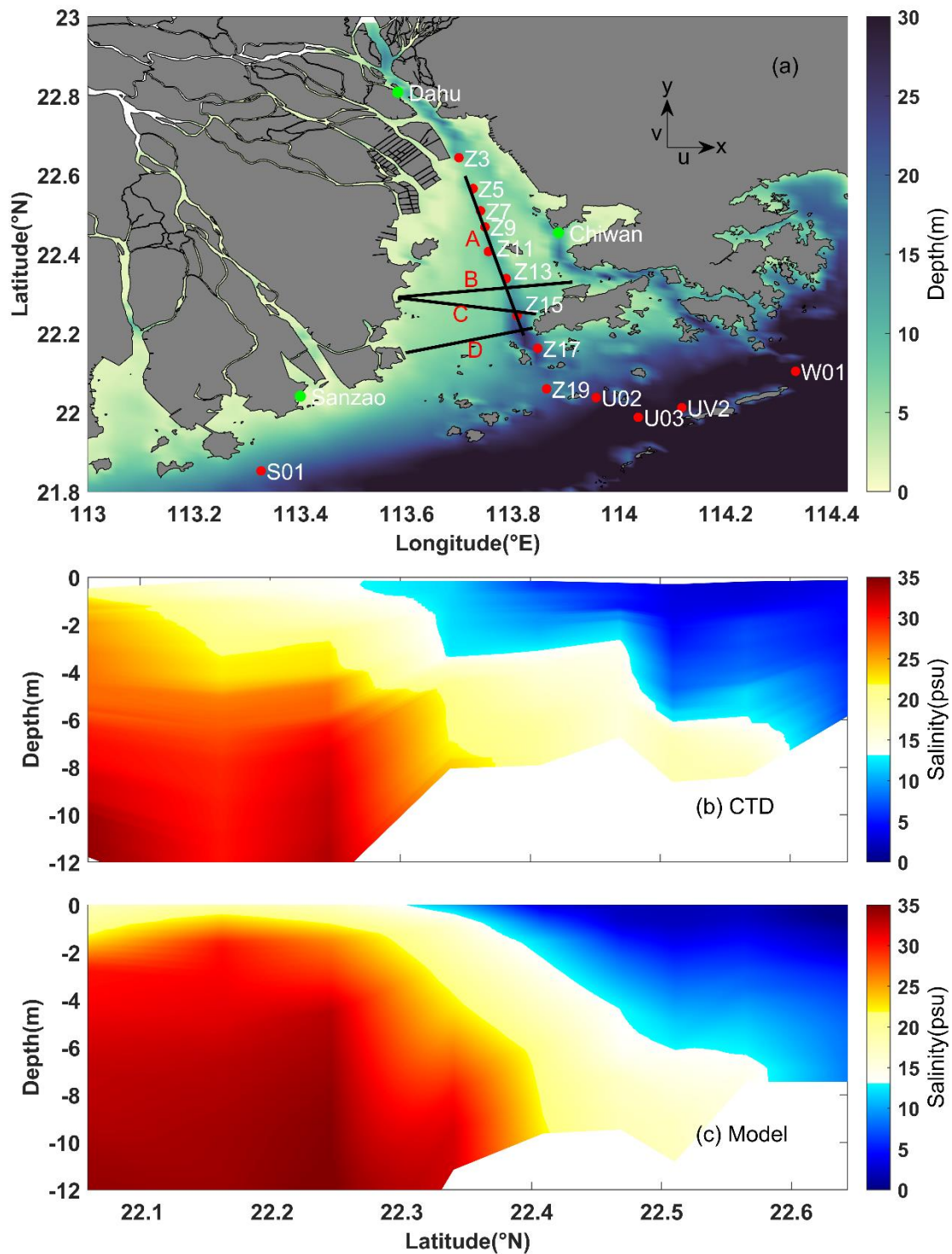
Figure 2 (a) Bathymetry of the model domain. Black lines mark sections for result analysis. Green dots

indicate tide gauge stations for elevation validation, and red dots indicate CTD positions for salinity

verification. **(b)** Along-estuary salinity profiles based on CTD depth-profiled data, closely aligned with

Section A; **(c)** salinity outputs from the numerical model.

308   Model verification involves comparing the model-derived sea surface elevation and

309   salinity with the corresponding observed values from the tide gauge and CTD stations,

310   respectively (Fig. 3). The observed sea surface elevation data are collected between 2 and 4

311   August 2017, and the observed salinity data are acquired through CTD profiling from 4 to 6

312   August 2017. A good agreement between the model and observed values highlights the

313   effectiveness of the model (Fig. 3). To further assess the model's performance, three statistical

314   parameters are calculated: the correlation coefficient (CC), Willmott Skill score (Willmott,

315   1981), and Root Mean Square Error (RMSE). These parameters quantify the model's accuracy

316   and skill:

$$CC = \frac{\sum_{i=1}^{N}(ob_i - \overline{ob})(mo_i - \overline{mo})}{\sqrt{\sum_{i=1}^{N}(ob_i - \overline{ob})^2 \sum_{i=1}^{N}(mo_i - \overline{mo})^2}}, \tag{4}$$

$$Skill = 1 - \frac{\sum_{i=1}^{N}(ob_i - mo_i)^2}{\sum_{i=1}^{N}(|mo_i - \overline{ob}| + |ob_i - \overline{ob}|)^2}, \tag{5}$$

$$and\ RMSE = \sqrt{\frac{1}{N}\sum_{i=1}^{N}(ob_i - mo_i)^2}, \tag{6}$$

317   where ob_i and mo_i are the observed data and model data, respectively, $\overline{ob}$ and $\overline{mo}$ are the

318   average value of the observed data and the model data, and N represents the number of

319   observations. The performance assessments of the modeled tidal elevation are presented in Fig.

320   3a–c. The model demonstrates a reasonable match with the observed tidal elevations,

321   exhibiting good performance with a skill score greater than 0.98, a correlation coefficient

322   exceeding 0.97, and a root mean square error less than 0.09 m. This indicates that the model

323   performs well in simulating tidal elevations. The assessments of the model's performance in

324   simulating salinity are depicted in Figs. 2b, c, and 3d–l. The correlation coefficients for salinity

325   are higher than 0.94, with the majority of skill scores exceeding 0.85 and root mean square

326   errors less than 3 psu. The model exhibits good performance in simulating salinity.
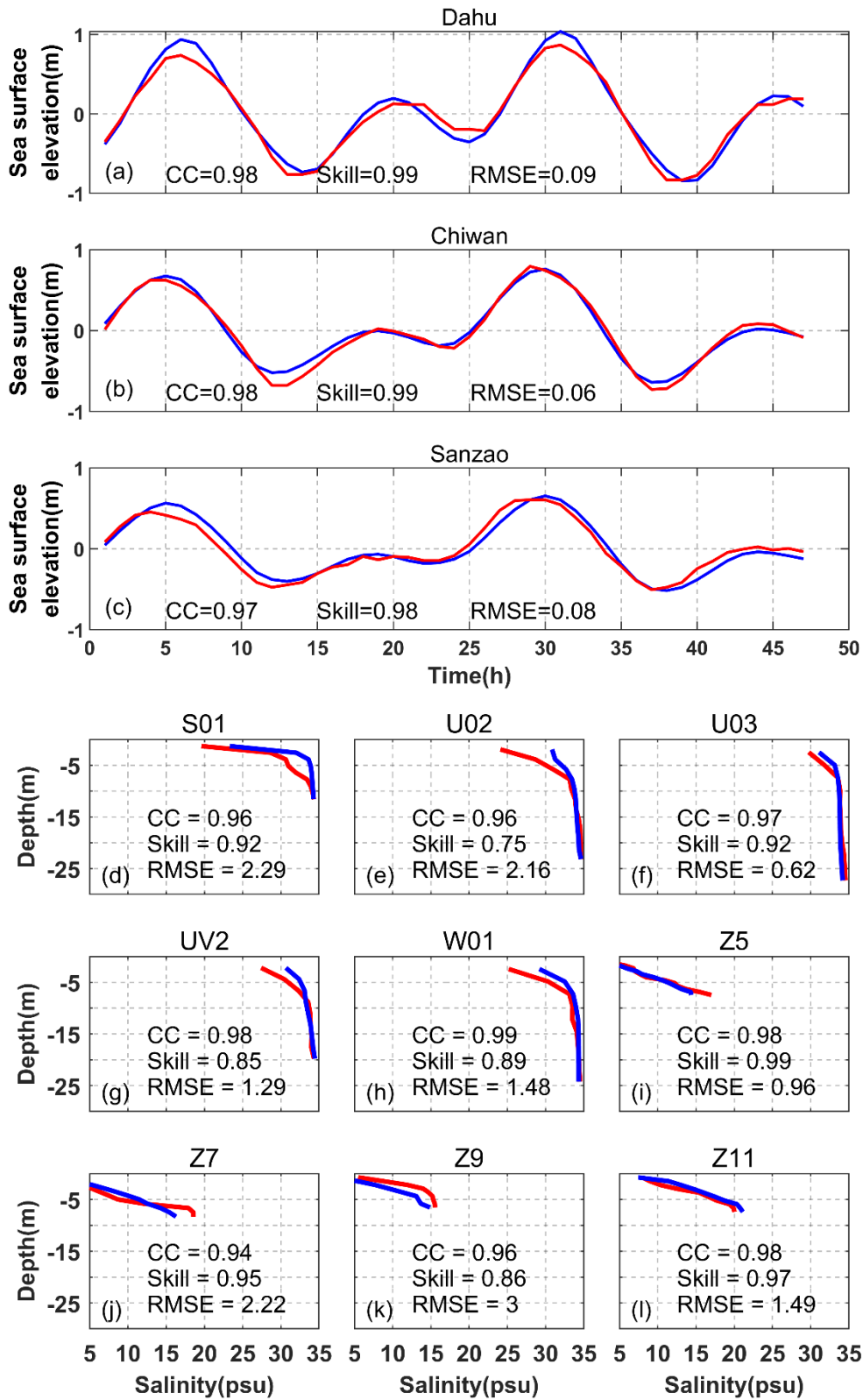
Figure 3 Comparisons between the observed (red line) and modeled (blue line) elevation and salinity. The three parameters including CC, Skill, and RMSE are calculated at each station.

3. Results

3.1 Contributions of dominant components for LRV

To quantify the contribution of each dynamic component of the LRV, the absolute values of each component are averaged throughout Section C in this study, as follows:

$$M(\cdot) = \frac{1}{B}\int abs(\cdot)dB, \tag{7}$$

where *abs* is the absolute value function, the symbol · can be replaced by each dynamic component of the LRV, and *B* represents the area of the cross-section.

Figure 4 illustrates the decomposition of cross-estuary LRV into dominant contributions for the reference case. During neap tides, the eddy viscosity component (u_{Ltu}) exhibits a two-layer structure with eastward flow in the upper layer and westward flow in the lower layer (Fig. 4a). The barotropic pressure gradient component (u_{Lba}) generally flows westward in most areas of the shoal, while it displays an eastward flow in the upper layer and a westward flow in the lower layer of the deep channel (Fig. 4b). The two-layer structure of u_{Lba} arises from the distinct trajectories of particles in the upper and lower layers. The integration results along these different trajectories produce varying magnitudes and opposite directions of u_{Lba} components in both layers. Conversely, the contribution from the baroclinic pressure gradient (u_{Lgr}; Fig. 4c) opposes u_{Lba}. During spring tides, the structure of the three components, namely u_{Ltu}, u_{Lba}, and u_{Lgr}, remains analogous to that during neap tides throughout the cross section (Fig. 4j–l). During both spring and neap tides, the three striking components (u_{Ltu}, u_{Lgr}, and u_{Lba}) are aggregated (Fig. 4e and n) and compared to the total LRV obtained directly from the model based on the Lagrangian particle tracking algorithms (Fig. 4d and m). It is observed that u_L primarily arises from an imbalance between u_{Ltu}, u_{Lgr}, and u_{Lba}. The eastward exchange circulation is predominantly attributed to u_{Ltu} in the upper layer of the shoal, while the westward flow in the lower layer of the shoal is primarily driven by u_{Ltu} and u_{Lba}. In the upper layer of

18

the deep channel, the eastward flow is determined by the interplay of u_{Lba} and u_{Ltu}, which also induces the westward flow in the lower layer of the channel. Notably, u_{Lgr} predominantly counteracts u_{Lba}.
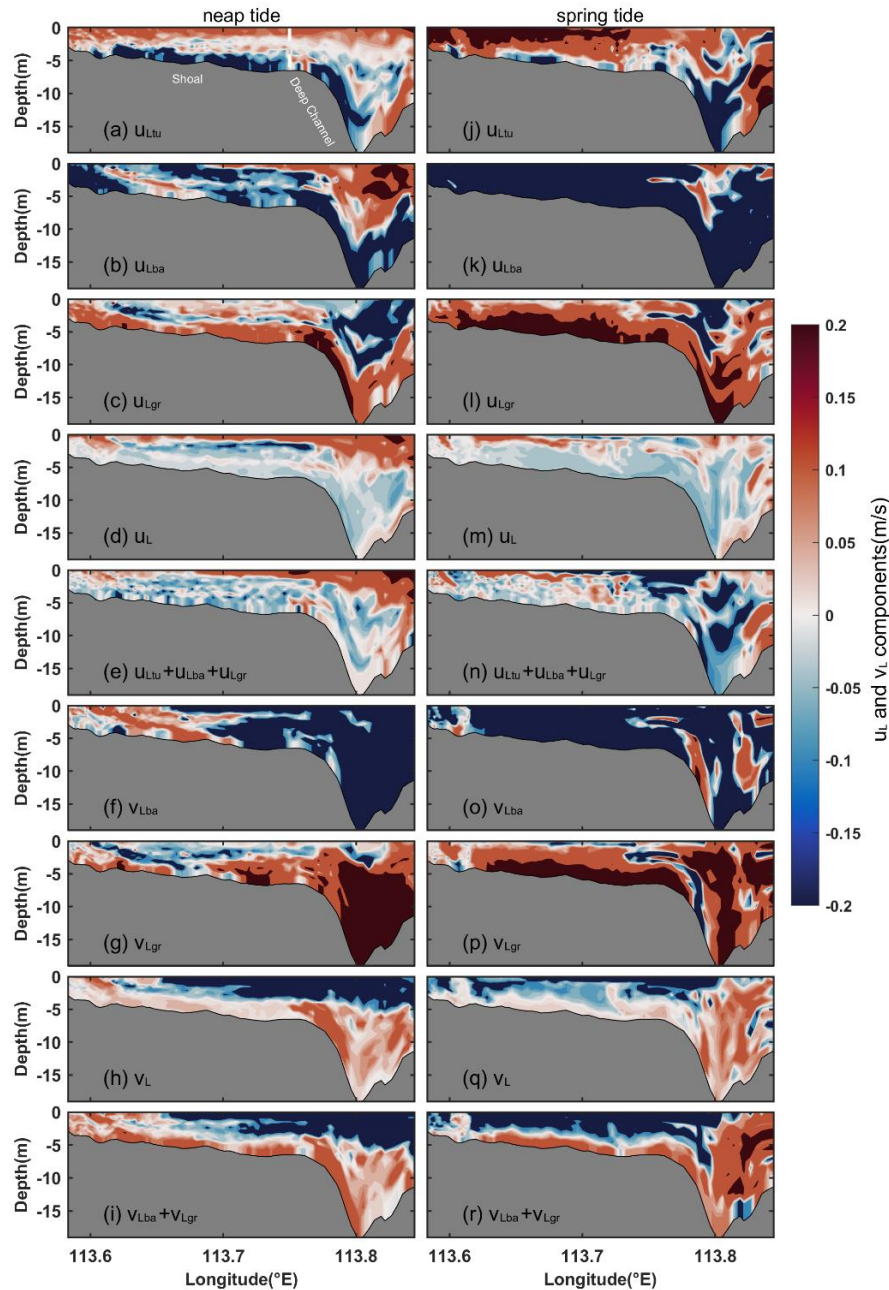

Figure 4 Dominant components of u_L and v_L in Section C for Case 1. For cross-estuary components: **(a, j)** eddy viscosity component (u_{Ltu}), **(b, k)** barotropic component (u_{Lba}), **(c, l)** baroclinic component (u_{Lgr}), **(d, m)** total LRV (u_L) directly obtained by the model, and **(e, n)** cumulative sum of u_{Ltu}, u_{Lba}, and u_{Lgr}. For along-estuary components: **(f, o)** barotropic pressure gradient component (v_{Lba}), **(g, p)** baroclinic pressure gradient

19

361   component (v_{Lgr}), **(h, q)** total LRV (v_L) obtained directly by the model, and **(i, r)** cumulative sum of v_{Lba} and

362   v_{Lgr}. The components during **(a–i)** represent neap tides, while those during **(j–r)** represent spring tides. For

363   cross-estuary components, red shading indicates eastward flow, and blue shading indicates westward flow.

364   For along-estuary components, red shading signifies inflow, while blue shading denotes outflow.

365   The decomposition of along-estuary LRV into dominant contributions is depicted in Fig.

366   4 for the reference case. During neap tides, the barotropic pressure gradient component (v_{Lba})

367   contributes to an up-estuary flow in most areas of the shoal and a down-estuary flow in the

368   deep channel (Fig. 4f); the baroclinic pressure gradient component (v_{Lgr}) exhibits a two-layer

369   circulation with the seaward flow in the upper layer and landward flow in the lower layer of

370   the shoal along with inflow in most areas of the deep channel (Fig. 4g). It shows the opposite

371   pattern to v_{Lba}. During spring tides, there is a down-estuary flow of v_{Lba} in the shoal, which is

372   contrary to the flow pattern during neap tides (Fig. 4o). Additionally, the outflow area of v_{Lgr}

373   in the upper layer of the shoal is smaller during spring tides than during neap tides (Fig. 4p).

374   Both during spring and neap tides, the sum of v_{Lba} and v_{Lgr} (Fig. 4i and r) closely resembles the

375   total along-estuary LRV (v_L; Fig. 4h and q). Therefore, the dominant components of v_L are v_{Lba}

376   and v_{Lgr}. Since these components must balance across the estuary, the outflow in the upper layer

377   is mainly determined by v_{Lba}, while the inflow in the lower layer is induced by v_{Lgr}.

378   The intensities of the exchange flows are quantified in Fig. 5 for the reference case. During

379   spring tides, the magnitude of u_{Ltu} is approximately 2 times higher than that during neap tides,

380   the magnitude of u_{Lgr} nearly doubles compared to that during neap tides, and the magnitude of

381   u_{Lba} is roughly 4 times as large as that during neap tides. Among the dominant components of

382   u_L, u_{Lba} exhibits the most pronounced contributions, being 1–2 times as strong as u_{Ltu} and u_{Lgr}.

383   During spring tides, the magnitudes of v_{Lba} and v_{Lgr} are about 1.4 times as large as those during

384   neap tides. The contributions from gravitational circulation and barotropic pressure gradient

385   component to total LRV are of the same magnitude.
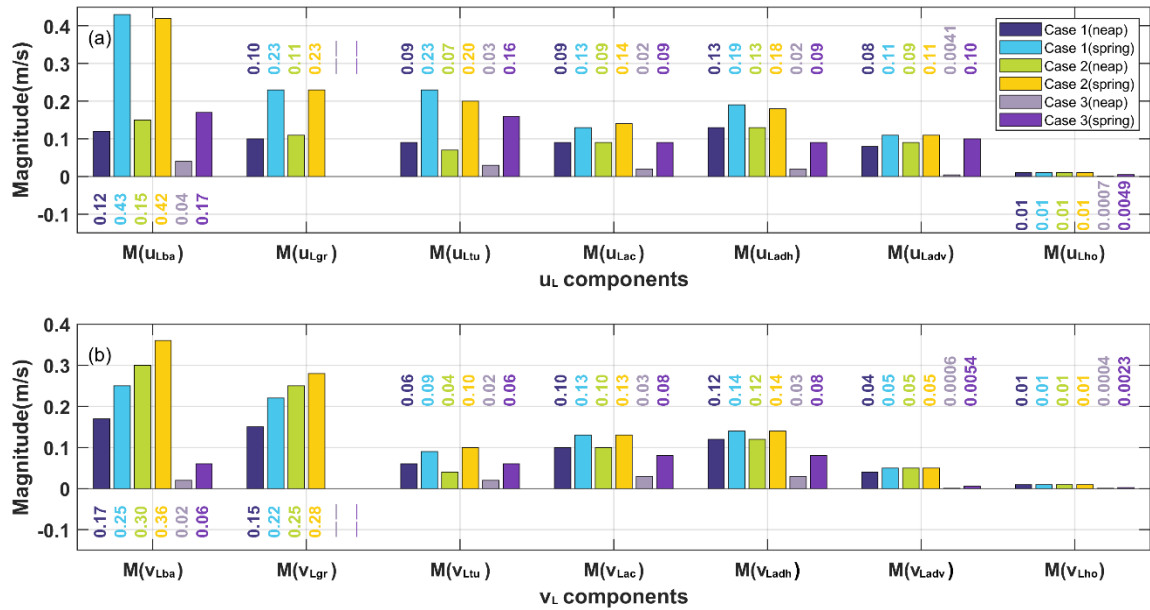
Figure 5 Bar charts for the magnitude of each component of u_L and v_L.

Neglecting the influence of wind, the cross-estuary and along-estuary dominant components are displayed in Fig. 6 for Case 2. The eddy viscosity component (u_{Ltu}) exhibits a similar pattern to the reference case both during neap and spring tides (Fig. 6a and j). However, during neap tides, the magnitude of the eastward flow of u_{Ltu} in the upper 2 m is approximately one order of magnitude smaller than that in Case 1 (Fig. 6a vs. Fig. 4a), although the absolute value of u_{Ltu} averaged in Section C for Case 2 is slightly different compared to that in Case 1 (Fig. 5). This suggests that wind primarily affects the upper exchange circulation by influencing the mixing of the upper water column. During spring tides, u_{Ltu} shows small differences in magnitude between Case 1 and Case 2 (Fig. 6j vs. Fig. 4j), indicating that wind sheds a slight influence on exchange flow during spring tides. During both spring and neap tides, the structures and magnitudes of the barotropic pressure gradient component (u_{Lba}; Fig. 6b and k) and the baroclinic pressure gradient component (u_{Lgr}; Fig. 6c and l) are similar to those in Case 1. When wind effects are not considered, the structure of the cross-estuary LRV (u_L) (Fig. 6d and m) is still determined by the combined contributions of u_{Lba}, u_{Lgr}, and u_{Ltu} (Fig. 6e and n).

21

However, the eastward flow determined by u_{Ltu} in the upper layer of the shoal in Case 1 transforms into a westward flow primarily driven by u_{Lba} in Case 2.
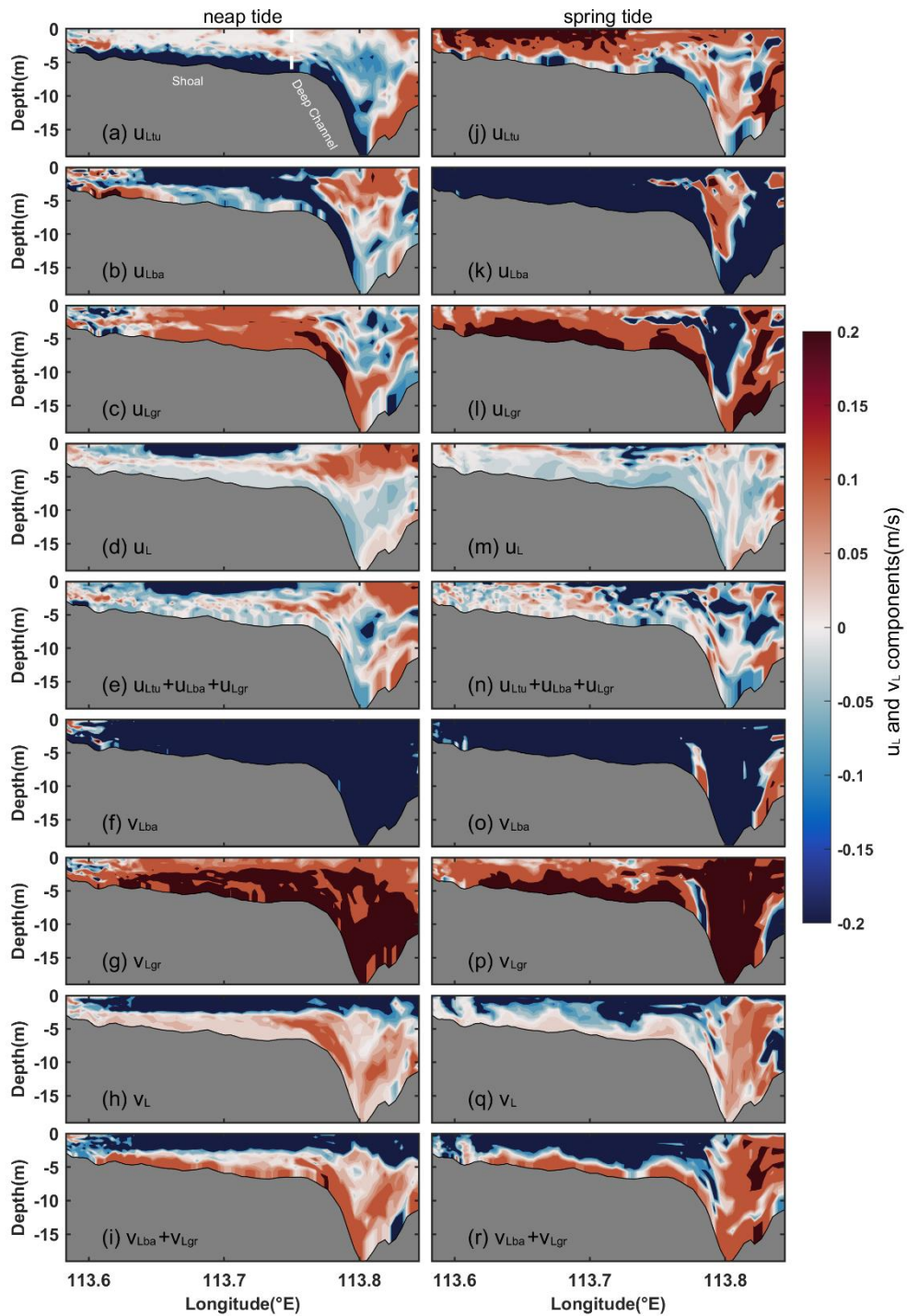

Figure 6 Same as Fig. 4, but for Case 2 without wind forcing.

The v_{Lba} changes from inflow in Case 1 to outflow in the shoal during neap tides (Fig. 6f). Similarly, v_{Lgr} shifts from outflow in Case 1 to inflow in the upper layer of the shoal during

22

409   neap tides in Case 2 (Fig. 6g). This suggests that wind plays a crucial role in the components

410   of LRV in the upper water column of the shoal. During spring tides, v_{Lba} and v_{Lgr} maintain the

411   same structure as observed in Case 1 (Fig. 6o and p), indicating that wind is unimportant during

412   spring tides. The structure of the along-estuary LRV (v_L) (Fig. 6h and q) is primarily determined

413   by the combined contributions of v_{Lba} and v_{Lgr} (Fig. 6i and r), analogous to that in Case 1. But

414   in the absence of wind, the magnitudes of v_{Lba} and v_{Lgr} are larger than those in Case 1, indicating

415   that southwesterly wind suppresses gravitational circulation. The relative contributions of v_{Lba}

416   and v_{Lgr} to v_L are approximately equal (Fig. 5).

417   The stratification and wind forcing are ignored in Case 3. The dominant components of

418   the cross-estuary LRV in Section C are shown in Fig. 7. During neap tides, the local

419   acceleration component (u_{Lac}) predominantly exhibits eastward flow in most areas, with minor

420   regions showing westward flow in the shoal and deep channel (Fig. 7a). Conversely, during

421   spring tides, a prevailing westward flow characterizes the majority of the shoal regions, while

422   an eastward flow prevails in the deep channel (Fig. 7g). These results highlight the profound

423   impact of tides on the structure of u_{Lac} in a homogeneous water column. Comparing the results

424   with those of Case 2, u_{Lac} undergoes a transition from vertically sheared flow in Case 2 to

425   horizontally sheared flow in Case 3, indicating that stratification plays a notable role in shaping

426   the structure of u_{Lac}. The horizontal nonlinear advective component (u_{Ladh}) exhibits a flow

427   pattern that is the reverse of u_{Lac} (Fig. 7b and h). The barotropic pressure gradient component

428   (u_{Lba}) primarily shows unidirectional westward flow throughout the cross section (Fig. 7c and

429   i). The pattern of u_{Lba} in the shoal and most of the lower layer of the deep channel is consistent

430   with that observed in Case 2. However, in the upper layer of the deep channel, u_{Lba} transforms

431   eastward flow in Case 2 into westward flow in Case 3. The eddy viscosity component (u_{Ltu})

432   induces a flow opposite to that of u_{Lba} (Fig. 7d and j), which differs from the vertically sheared

433   flow observed in Case 2.
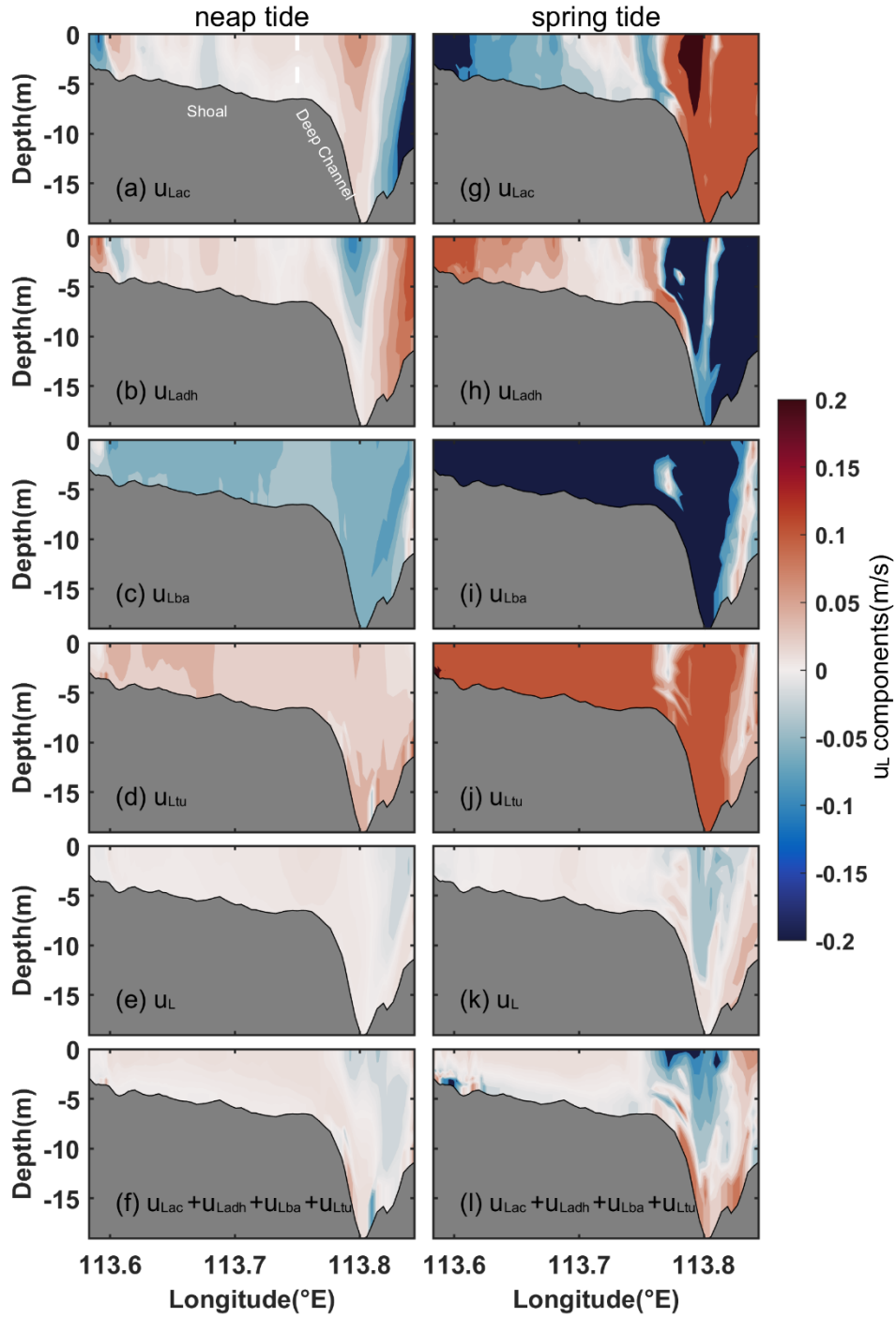
Figure 7 Dominant components of u_L in Section C for Case 3. **(a, g)** Local acceleration component (u_{Lac}),
(b, h) horizontal nonlinear advection component (u_{Ladh}), **(c, i)** barotropic pressure gradient component (u_{Lba}),
(d, j) eddy viscosity component (u_{Ltu}), **(e, k)** the total LRV (u_L) obtained directly by the model, and **(f, l)** the
sum of u_{Lac}, u_{Ladh}, u_{Lba}, and u_{Ltu} during **(a–f)** neap and **(g–l)** spring tides, respectively. Red shading represents
eastward flow and blue shading represents westward flow.

440   The structure of the cross-estuary LRV (u_L) (Fig. 7e and k) closely resembles the structure

441   of the sum of the four components: u_{Lac}, u_{Ladh}, u_{Lba}, and u_{Ltu} in Case 3 (Fig. 7f and l). This

442   indicates that the overall structure of u_L (Fig. 7e and k) is primarily determined by the combined

443   effects of these four components. Among them, the eastward flow in the shoal and the lower

444   layer of the deep channel is mainly determined by u_{Ltu} (Fig. 7d and j), with u_{Lac} playing a

445   secondary role (Fig. 7a and g). On the other hand, the westward flow in the upper layer of the

446   deep channel is primarily influenced by u_{Lba} (Fig. 7c and i), with u_{Ladh} contributing as a

447   secondary component (Fig. 7b and h).

448   The magnitudes of u_{Lac}, u_{Ladh}, and u_{Lba} during spring tides are approximately four times

449   as large as those during neap tides in Case 3 (Fig. 5). The magnitude of u_{Ltu} during spring tides

450   is approximately fivefold compared to neap tides. The relative contributions of u_{Lba} and u_{Ltu} to

451   u_L are roughly equal, and u_{Lac} and u_{Ladh} have similar contributions. Moreover, the contribution

452   of u_{Lba} is approximately 1–2 times as large as that of u_{Lac} in Case 3.

453   Both during spring and neap tides, the along-estuary barotropic pressure gradient

454   component (v_{Lba}) exhibits outflow in most areas in Case 3 (Fig. 8a and e), which is similar to

455   Case 2, indicating that stratification has minimal effects on the structure of v_{Lba}. The eddy

456   viscosity component (v_{Ltu}) shows a nearly opposite pattern compared to v_{Lba} (Fig. 8b and f).

457   Compared to Case 2, v_{Ltu} exhibits an opposite pattern at the bottom of the shoal and in the deep

458   channel. The imbalance between the two components, v_{Lba} and v_{Ltu} (Fig. 8d and h), determines

459   the along-estuary circulation (v_L) (Fig. 8c and g). The inflow in the shoal is primarily driven by

460   v_{Ltu}, while the outflow in the deep channel is dominated by v_{Lba}. During spring tides, the

461   magnitudes of v_{Lba} and v_{Ltu} are about 3-fold that during neap tides in Case 3 (Fig. 5). During

462   neap and spring tides, the relative contributions of v_{Lba} and v_{Ltu} to v_L are equal.
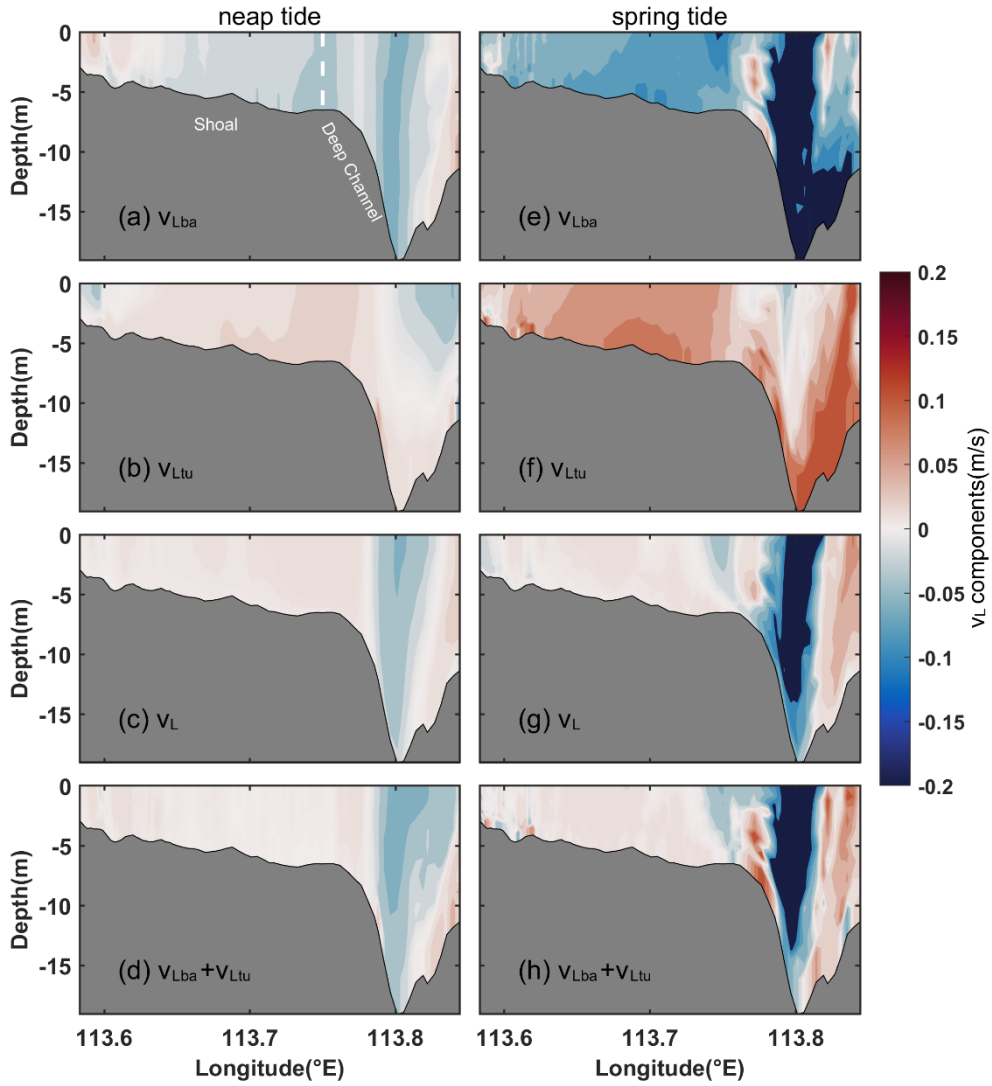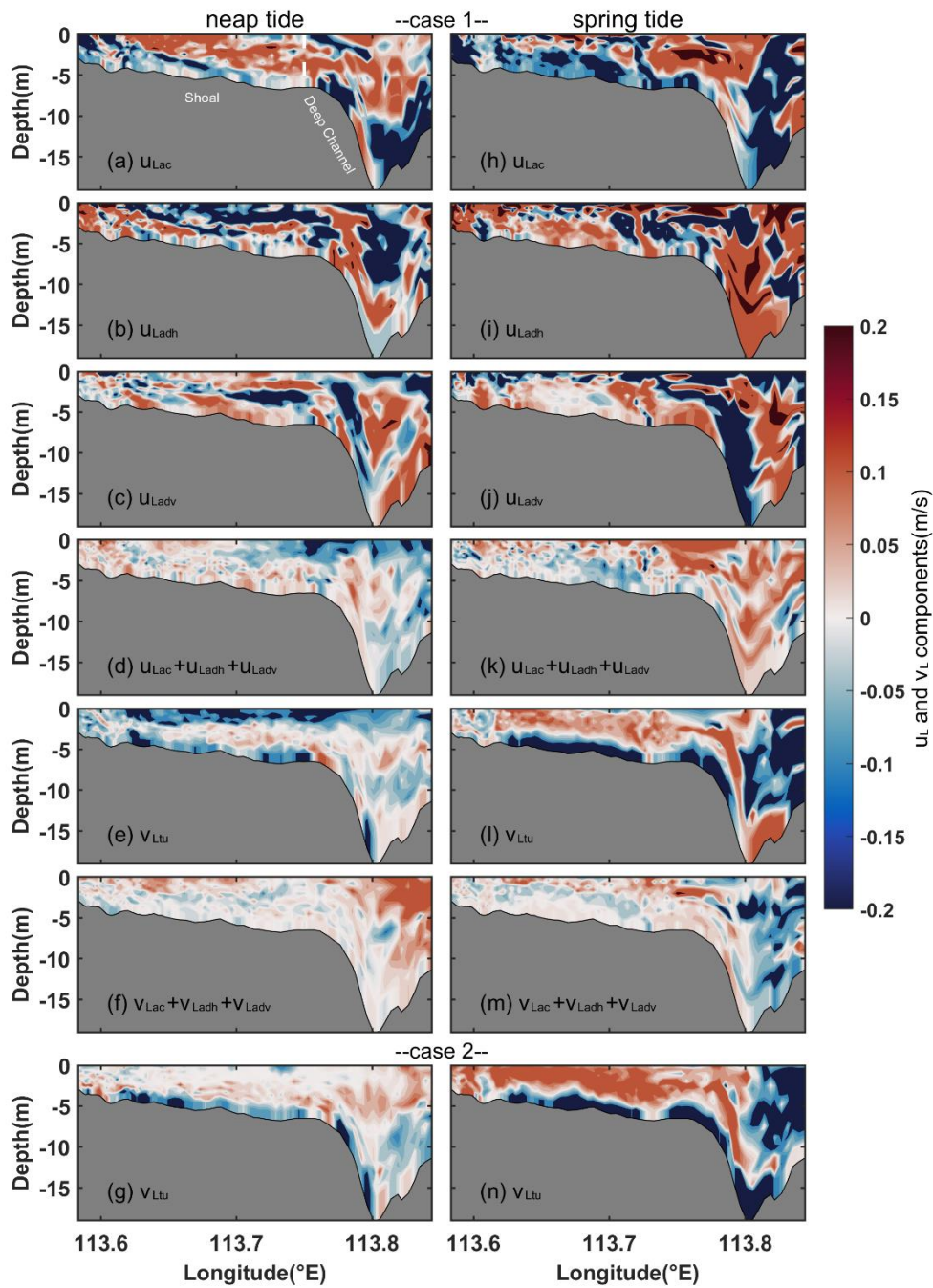
Figure 8 Dominant components of v_L in Section C for Case 3. **(a, e)** Barotropic pressure gradient component (v_{Lba}), **(b, f)** eddy viscosity component (v_{Ltu}), **(c, g)** total LRV obtained directly by the model, and **(d, h)** the sum of v_{Lba} and v_{Ltu} during **(a–d)** neap and **(e–h)** spring tides, respectively. Red shading represents inflow, and blue shading represents outflow.

3.2 Contributions of Non-dominant Components for LRV

The analysis of the contributions from non-dominant components to LRV for Case 1 is depicted in Fig. 9. During neap tides, the local acceleration (u_{Lac}) induces eastward flow in the majority of the upper layer and westward flow in the lower layer (Fig. 9a). Conversely, the horizontal nonlinear advection component (u_{Ladh}) exhibits an opposite pattern to u_{Lac} across

26

473   most regions (Fig. 9b). Meanwhile, the vertical nonlinear advective component (u_{Ladv}) serves

474   as a sandwiched structure, characterized by vertically staggered eastward and westward flow

475   (Fig. 9c). The combined configuration of u_{Lac} and u_{Ladh} contrasts with that of u_{Ladv}, yielding a

476   relatively small and negative contribution from the sum of these three components (Fig. 9d) to

477   u_L (Fig. 4d). Consequently, the three components are denoted as non-dominant components.

478   The magnitudes of the non-dominant components of u_L during spring tides are slightly larger

479   than those during neap tides. The general patterns of these three components during spring tides

480   resemble those during neap tides except for some areas (Fig. 9h–j). Moreover, both during

481   spring and neap tides, the horizontal diffusion component (u_{Lho}) is smaller compared to the

482   other components (not shown), and its contribution is negligible. For along-estuary non-

483   dominant components, the combination of the local acceleration component (v_{Lac}), the

484   horizontal nonlinear advective component (v_{Ladh}), and the vertical nonlinear term (v_{Ladv}) (Fig.

485   9f) contributes to total LRV (Fig. 4h) less and negatively during neap tides. Additionally, the

486   eddy viscosity-induced flow (v_{Ltu}) during neap tides exhibits a vertical shear structure, with

487   outflow in the upper and lower layer and inflow in the middle layer (Fig. 9e). During spring

488   tides, the overall structures for each non-dominant component slightly differ from those during

489   neap tides except for some upper areas and the magnitudes during spring tides exceed those

490   recorded during neap tides (Fig. 9l and m). For both spring and neap tides, the contributions of

491   the horizontal diffusion components (v_{Lho}) are negligible (not shown). Moreover, the

492   contribution of v_{Ltu} is relatively smaller compared to their respective dominant components (Fig.

493   5). In the absence of wind effects, the structure and contribution of each non-dominant

494   component of the LRV in Case 2 closely resemble those observed in Case 1 during both spring

495   and neap tides (not shown), with the exception of the noticeably reduced along-estuary eddy

496   viscosity component (v_{Ltu}) by one order of magnitude in the upper layer in Case 2 during neap

497   tides (Fig. 9g) and slightly intensified during spring tides (Fig. 9n) compared to scenarios with
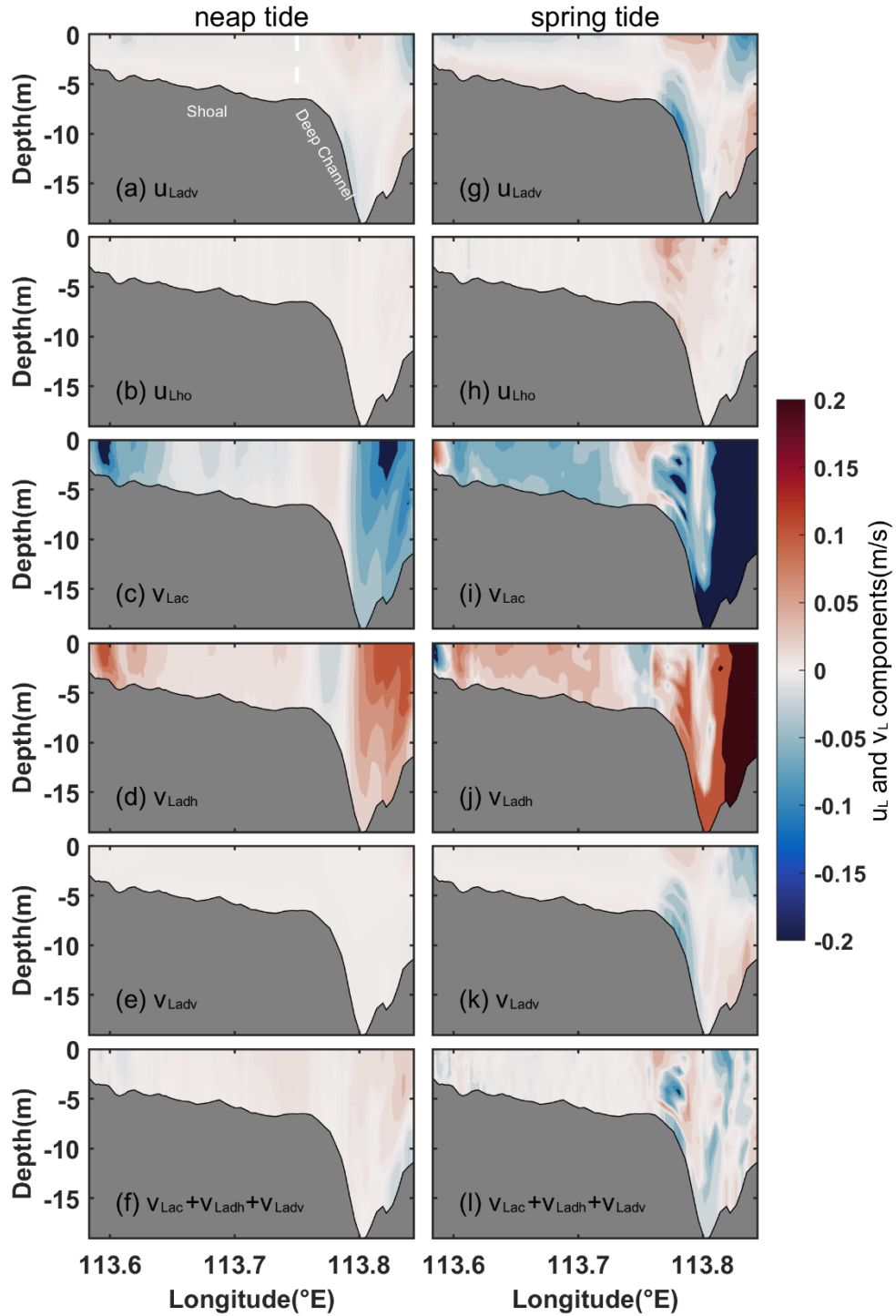
498

Figure 9 Non-dominant components of u_L and v_L in Section C for Cases 1 and 2. For cross-estuary components in Case 1: **(a, h)** local acceleration component (u_{Lac}), **(b, i)** horizontal nonlinear advection component (u_{Ladh}), **(c, j)** vertical nonlinear advection component (u_{Ladv}), and **(d, k)** the sum of u_{Lac}, u_{Ladh}, and u_{Ladv} during **(a–d)** neap and **(h–k)** spring tides, respectively; for along-estuary components in Case 1: **(e, l)** eddy viscosity component (v_{Ltu}), **(f, m)** the sum of v_{Lac}, v_{Ladh}, and v_{Ladv} during **(e, f)** neap and **(l, m)** spring tides, respectively. Along-estuary **(g, n)** eddy viscosity component (v_{Ltu}) in Case 2 during **(g)** neap and **(n)** spring tides, respectively. The shading follows the same indications as presented in Fig. 1.

506 wind. These indicate that wind has a weak influence on the non-dominant components of cross-

507 estuary circulation except for v_{Ltu}.

508   Neglecting wind forcing and stratification, the magnitudes of the vertical nonlinear

509 advection component (u_{Ladv}) and horizontal diffusion component (u_{Lho}) are relatively low

510 during both spring and neap tides. Compared to Case 2, the magnitude of u_{Lho} (Fig. 10b and h)

511 in Case 3 is reduced by approximately half during spring tides and by a factor of 14 during

512 neap tides, while the magnitude of u_{Ladv} (Fig. 10a) in Case 3 experiences an approximately

513 twentyfold reduction during neap tides (Fig. 5). For both neap and spring tides, v_{Lac} shifts from

514 inflow in Case 2 to outflow in Case 3 in some areas of the shoal (Fig. 10c and i). The horizontal

515 nonlinear advection component (v_{Ladh}) in Case 3 exhibits a pattern opposite to that of v_{Lac} (Fig.

516 10d and j). Their combined contributions of these two components to total LRV can be

517 disregarded (Fig. 10f and l). The contributions from the vertical nonlinear advection component

518 (v_{Ladv}; Fig. 10e and k) and horizontal diffusion component (v_{Lho}; not shown) during spring and

519 neap tides remain relatively low in Case 3. The magnitude of v_{Lho} in Case 3 is approximately

520 fivefold smaller during spring tides and 25 times smaller during neap tides than those in Case

521 2, while the magnitude of v_{Ladv} in Case 3 experiences an approximately tenfold reduction during

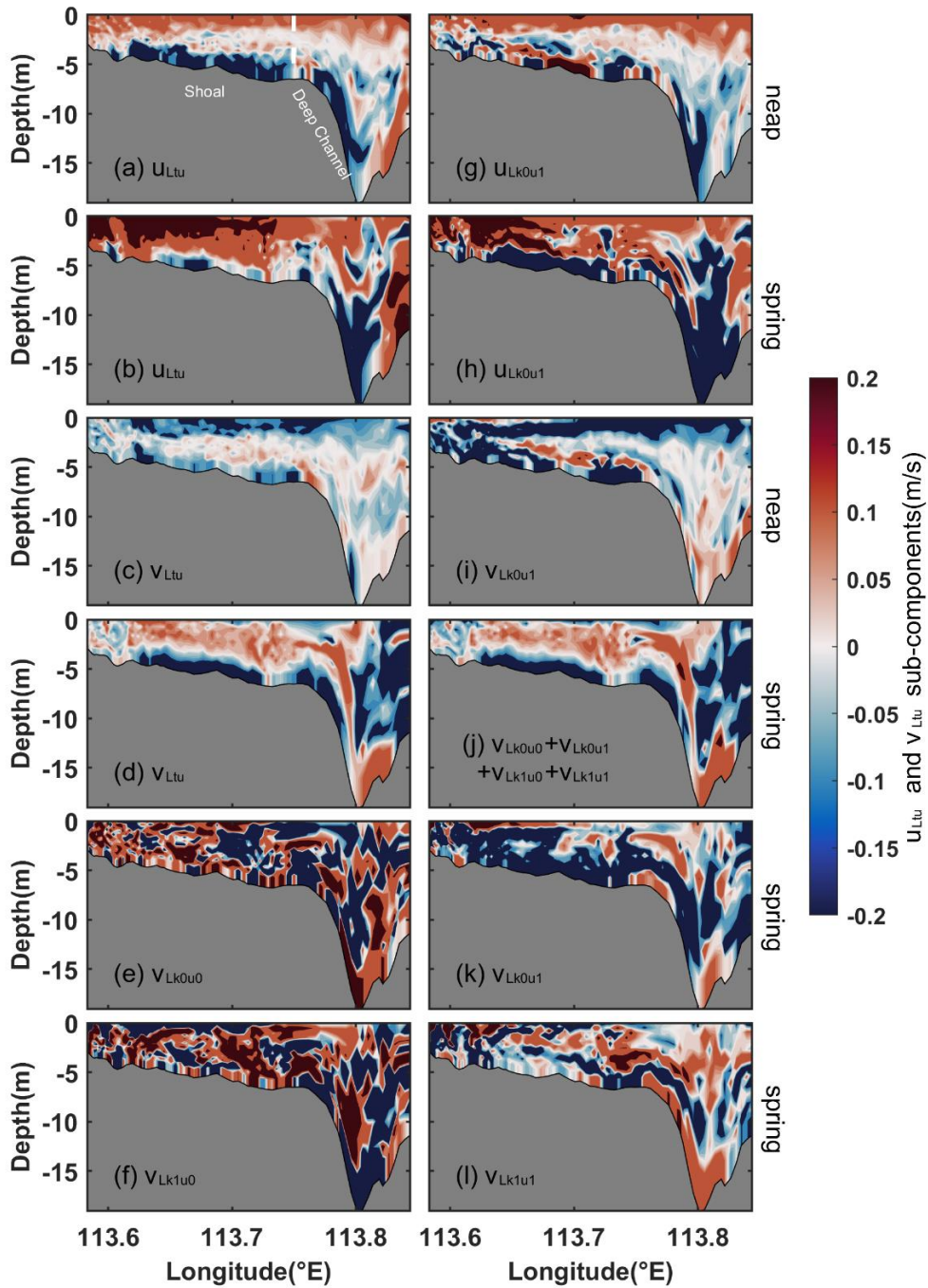522 spring tides and an eightyfold reduction during neap tides compared to Case 2 (Fig. 5).

Figure 10 Non-dominant components of u_L and v_L in Section C for Case 3. For cross-estuary components: **(a, g)** vertical nonlinear advection component (u_{Ladv}), **(b, h)** horizontal diffusion component (u_{Lho}); for along-estuary components: **(c, i)** local acceleration component (v_{Lac}), **(d, j)** horizontal advection component (v_{Ladh}), **(e, k)** vertical advection component (v_{Ladv}), and **(f, l)** the sum of v_{Ladc}, v_{Ladh} and v_{Ladv}, during **(a–f)** neap and **(g–l)** spring tides, respectively. The shading follows the same indications as presented in Fig. 1.

3.3 Contributions of dominant components for the eddy viscosity component

Through an analysis of dominant mechanisms influencing LRV under various dynamic factors, the findings indicate that the cross-estuary eddy viscosity component modulates the configuration of the cross-estuary LRV. In the upper layers, this component exhibits an enhancement of an order of magnitude under the influence of the dominant southwesterly winds, relative to conditions in the absence of wind in the PRE. However, the along-estuary eddy viscosity component is not the predominant contributor to along-estuary LRV under stratified circumstances. In the case of destratification, both the along-estuary and cross-estuary eddy viscosity components play roles in shaping the total LRV. A comprehensive exploration of the dominant mechanisms of the eddy viscosity component entails further decompositions of both the along-estuary and cross-estuary eddy viscosity components into four subgroups. This analysis provides general conclusions and implications for future studies. These subgroups encompass the coupled component of tidal-averaged eddy viscosity and velocity gradient oscillation, the tidal straining component, the turbulent mean component, and the coupled component of tidal-averaged velocity gradient and eddy viscosity oscillation.

During neap tides, the cross-estuary turbulent mean component (u_{Lk0u1}) for Case 1 displays eastward flows in the upper layer and westward flows in the lower layer (Fig. 11g). During spring tides, u_{Lk0u1} closely resembles the pattern observed during neap tides (Fig. 11h). The structure of u_{Lk0u1} during neap and spring tides is identical to that of the eddy viscosity (u_{Ltu}) (Fig. 11a and b). Therefore, u_{Ltu} is predominantly influenced by u_{Lk0u1}. During neap tides, the along-estuary turbulent mean component (v_{Lk0u1}) for Case 1 exhibits a three-layer structure in the shoal, with outflow occurring in the surface and bottom layers, and inflow in the middle layer (Fig. 11i). In the deep channel, there is a two-layer flow pattern with outflow in the upper layer and inflow in the lower layer. This structure aligns with that of the eddy viscosity component (v_{Ltu}) (Fig. 11c). Hence, during neap tides, v_{Ltu} is primarily influenced by v_{Lk0u1}.

31

554   During spring tides, the structure of v_{Ltu} for Case 1 (Fig. 11d) is contributed by the combined

555   effect of the four components: v_{Lk0u0}, v_{Lk0u1}, v_{Lk1u0}, and v_{Lk1u1} (Fig. 11j), which differs from the

556   structure observed during neap tides. The inflow occurring in the upper layer of the shoal is

557   primarily determined by v_{Lk0u0} and v_{Lk1u0} (Fig. 11e and f), and the outflow in the lower layer of

558   the shoal is mainly influenced by v_{Lk0u1} (Fig. 11k). The structure in the deep channel is primarily

559   determined by v_{Lk0u1}.

Figure 11 Vertical section of cross-estuary (u_{Ltu}) and along-estuary (v_{Ltu}) eddy viscosity components along with their corresponding dominant subcomponents in Section C for Case 1. The u_{Ltu} during **(a)** neap and **(b)** spring tides, and **(g, h)** the corresponding turbulent mean component (u_{Lk0u1}). **(c)** v_{Ltu} and **(i)** the corresponding turbulent mean component (v_{Lk0u1}) during neap tides, and **(d)** v_{Ltu} and **(j)** the sum of four dominant subcomponents **(e, f, k, and l)** during spring tides. The shading follows the same indications as presented in Fig. 1.

567   During neap tides, the cross-estuary turbulent mean component (u_{Lk0u1}) for Case 2 exhibits

568   eastward flow in the upper layer and westward flow in the lower layer (Fig. 12b). This pattern

569   aligns with Case 1. However, the magnitude of the eastward flow in the upper layer of u_{Lk0u1}

570   during neap tides is one order of magnitude smaller than that observed in Case 1. During spring

571   tides, the structure and magnitude of u_{Lk0u1} for Case 2 are similar to those of Case 1 (Fig. 12j),

572   suggesting a weak influence of wind on u_{Lk0u1}. Similar to Case 1, both during neap and spring

573   tides, the cross-estuary eddy viscosity component (u_{Ltu}) (Fig. 12a and i) is predominantly

574   determined by u_{Lk0u1} (Fig. 12b and j). During neap tides, the along-estuary turbulent mean

575   component (v_{Lk0u1}) for Case 2 exhibits inflow in the upper layer and outflow in the lower layer

576   (Fig. 12d). The structure of v_{Lk0u1} in the lower layer is consistent with that in Case 1, while the

577   structure in the upper layer is opposite to that of Case 1. Without the influence of wind, the

578   structure of v_{Lk0u1} in the upper layer shifts from outflow in Case 1 to inflow. During spring tides,

579   the area and magnitude of inflow in the upper layer of v_{Lk0u1} for Case 2 are larger than those

580   during neap tides (Fig. 12l). Both during neap and spring tides, the along-estuary eddy viscosity

581   component (v_{Ltu}) (Fig. 12c and k) exhibits the same structure as v_{Lk0u1} (Fig. 12d and l). Hence,

582   v_{Ltu} is predominantly influenced by the turbulent mean component (v_{Lk0u1}).

583   Without consideration of stratification, the cross-estuary tidal straining component (u_{Lk1u0})

584   for Case 3 exhibits eastward flow (Fig. 12f) in the shoal during neap tides. The u_{Lk1u0} undergoes

585   a transition from westward flow in Case 2 to eastward flow in the lower layer. During spring

586   tides, the u_{Lk1u0} for Case 3 maintains the same pattern as observed during neap tides, and its

587   magnitude is greater than that during neap tides (Fig. 12n). During neap tides, the along-estuary

588   tidal straining component (v_{Lk1u0}) for Case 3 exhibits inflow in most areas of the shoal and

589   shows a two-layer structure in the deep channel with outflow in the upper layer, and inflow in

590   the lower layer (Fig. 12h), which is analogous to the structure of v_{Lk1u0} in the shoal in Case 2.

591   Stratification mainly affects the structure of v_{Lk1u0} in the lower layer of the deep channel. During

34

592 spring tides, the inflow area of v_{Lk1u0} for Case 3 in the deep channel is larger than that during

593 neap tides (Fig. 12p). During both neap and spring tides, the u_{Ltu} and v_{Ltu} (Fig. 12e, g, m, and

594 o) align with u_{Lk1u0} and v_{Lk1u0} (Fig. 12f, h, n, and p), respectively. Hence, u_{Ltu} and v_{Ltu} are

595 primarily influenced by u_{Lk1u0} and v_{Lk1u0}, differing from the dominant components in Case 2.

596 Without consideration of stratification, the dominant components of u_{Ltu} and v_{Ltu} shift from the

597 turbulent mean components (u_{Lk0u1} and v_{Lk0u1}) in Case 2 to the tidal straining components (u_{Lk1u0}

598 and v_{Lk1u0}) in Case 3. During neap tides, the magnitude of u_{Lk1u0} is approximately 5 times

599 smaller than that in Case 2, while the magnitude of v_{Lk1u0} is around 14 times smaller than that

600 in Case 2 (Table 2). During spring tides, the magnitude of u_{Lk1u0} is roughly 4 times smaller than

601 that in Case 2, and the magnitude of v_{Lk1u0} is approximately 6 times smaller than that in Case

602 2.

603 **Table 2** The magnitude of each subcomponent for the total eddy viscosity component in three scenarios.

|	Case 1 (neap)	Case 1 (spring)	Case 2 (neap)	Case 2 (spring)	Case 3 (neap)	Case 3 (spring)
$M(u_{Lk0u0})$	0.16	0.42	0.14	0.42	0.001	0.068
$M(u_{Lk0u1})$	0.11	0.27	0.07	0.20	0.006	0.010
$M(u_{Lk1u0})$	0.16	0.46	0.14	0.43	0.031	0.103
$M(u_{Lk1u1})$	0.08	0.17	0.04	0.16	0.001	0.003
$M(v_{Lk0u0})$	0.15	0.30	0.11	0.28	0.005	0.023
$M(v_{Lk0u1})$	0.11	0.19	0.07	0.15	0.011	0.032
$M(v_{Lk1u0})$	0.16	0.37	0.11	0.28	0.008	0.044
$M(v_{Lk1u1})$	0.11	0.20	0.05	0.13	0.001	0.004

604
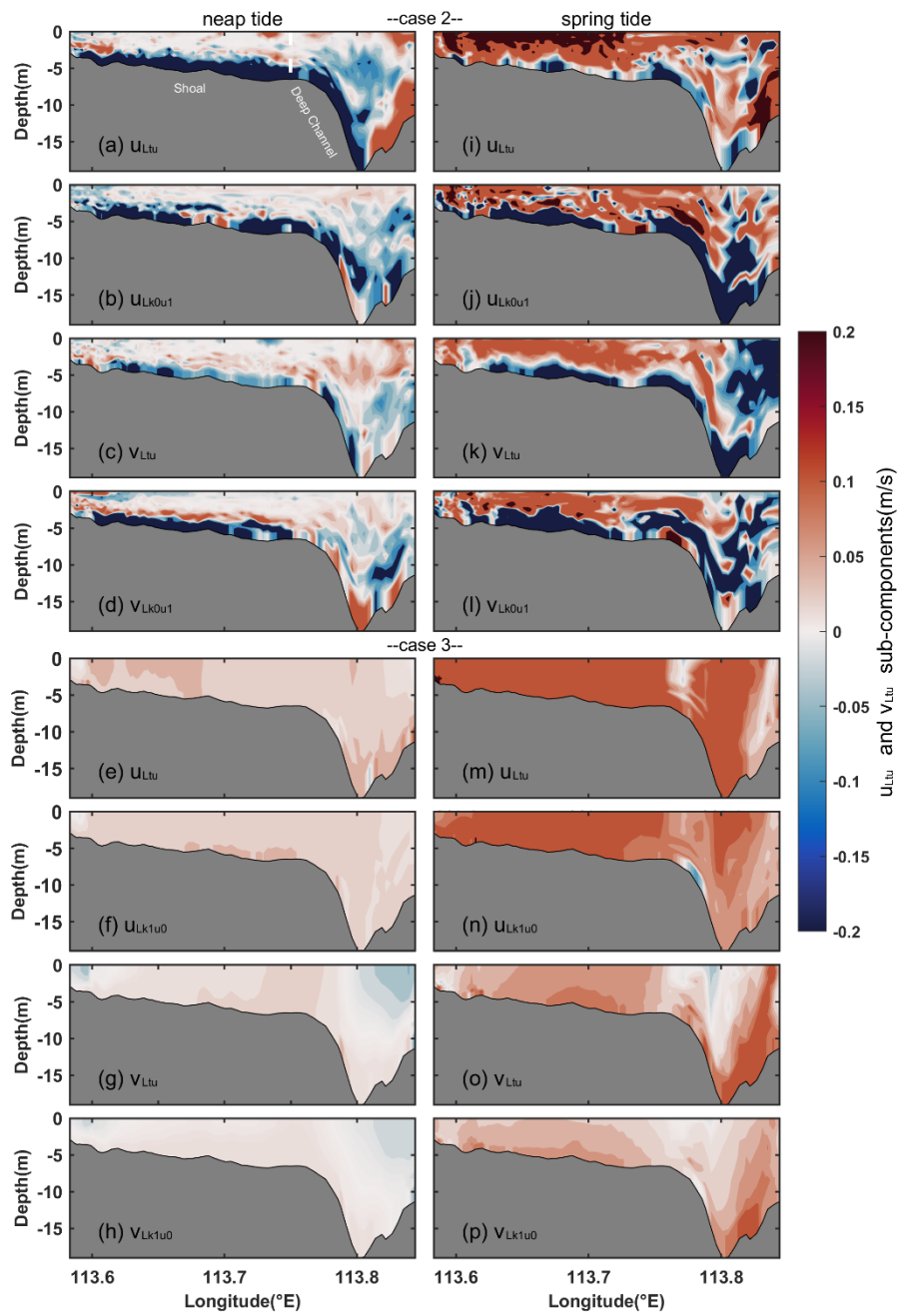
Figure 12 The structure of cross-estuary (u_{Ltu}) and along-estuary (v_{Ltu}) eddy viscosity components and the corresponding dominant components in Section C for Cases 2 **(a–d and i–l)** and 3 **(e–h, and m–p)**. For Case 2: the u_{Ltu} during **(a)** neap and **(i)** spring tides, and **(b, j)** the corresponding turbulent mean component (u_{Lk0u1}); the v_{Ltu} during **(c)** neap and **(k)** spring tides, and **(d, l)** the corresponding turbulent mean component (v_{Lk0u1}). For Case 3: the u_{Ltu} during **(e)** neap and **(m)** spring tides, and **(f, n)** the corresponding tidal straining component (u_{Lk1u0}); the v_{Ltu} during **(g)** neap and **(o)** spring tides, and **(h, p)** the corresponding tidal straining component (v_{Lk1u0}). The shading follows the same indications as presented in Fig. 1.

3.4 Contributions of non-dominant components for eddy viscosity component

During neap tides, the cross-estuary coupled component of the tidal-averaged eddy viscosity and velocity gradient oscillation (u_{Lk0u0}) for Case 1 demonstrates a vertically sheared structure in the shoal, with alternating westward and eastward flows (Fig. 13a). During spring tides, u_{Lk0u0} for Case 1 predominantly flows eastward in the shoal and displays a two-layer structure in the deep channel with eastward flow in the upper layer and westward flow in the lower layer (Fig. 13c). The cross-estuary tidal straining component (u_{Lk1u0}) during neap tides exhibits an opposing structure to that of u_{Lk0u0} in the lower layer (Fig. 13g). In the upper layer, it displays a similar pattern to u_{Lk0u0}. During spring tides, the extent and magnitude of the eastward flow of u_{Lk1u0} in the deep channel are larger than during neap tides (Fig. 13i). During neap tides, the cross-estuary coupled component of the eddy viscosity oscillation and the tidal-averaged velocity gradient (u_{Lk1u1}) exhibits a complex vertically sheared structure (Fig. 13b). During spring tides, u_{Lk1u1} displays a similar structure but with a greater magnitude than that during neap tides (Fig. 13d). The combined effect of the three components (Fig. 13h and j), namely u_{Lk0u0}, u_{Lk1u0}, and u_{Lk1u1}, contrasts with u_{Lk0u1} (Fig. 11g and h) in most areas of cross section.

During neap tides, the along-estuary coupled component of the tidal-averaged eddy viscosity and velocity gradient oscillation (v_{Lk0u0}) exhibits a vertically sheared structure with alternating outflow and inflow in Case 1 (Fig. 13e). The structure of the along-estuary tidal straining component (v_{Lk1u0}) closely resembles that of v_{Lk0u0} in the upper layer of the shoal, while it is opposite in the lower layer of the shoal and deep channel (Fig. 13k). Additionally, the cross-estuary coupled component of the eddy viscosity oscillation and the tidal-average velocity gradient (v_{Lk1u1}) displays an opposite pattern to v_{Lk0u0} in the upper layer of the shoal (Fig. 13f). The combined effects of the three along-estuary non-dominant components (Fig. 13l) are opposite to the dominant component (v_{Lk0u1}; Fig. 11i) and exert a negative contribution to
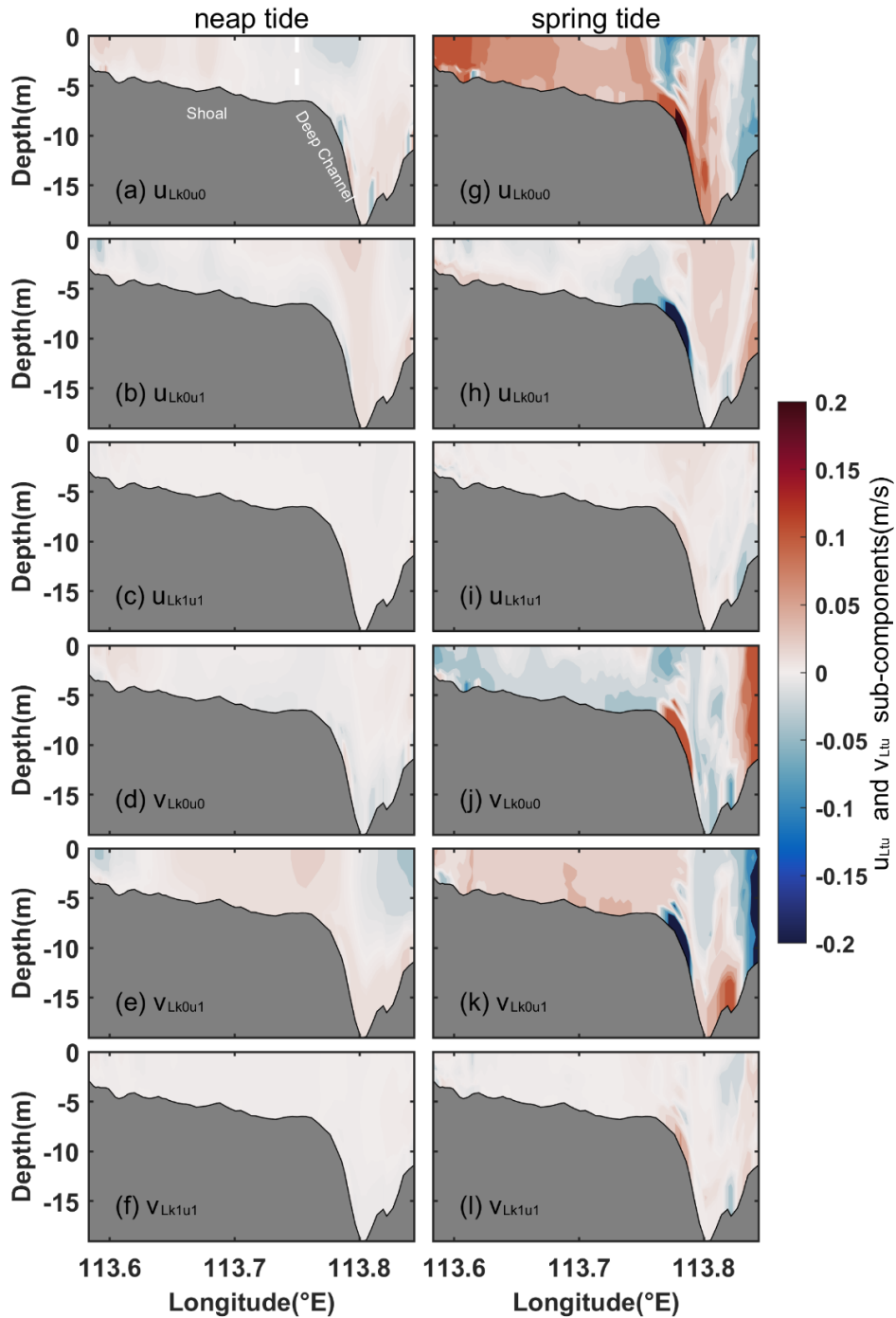
37

the total eddy viscosity component (Fig. 11c).
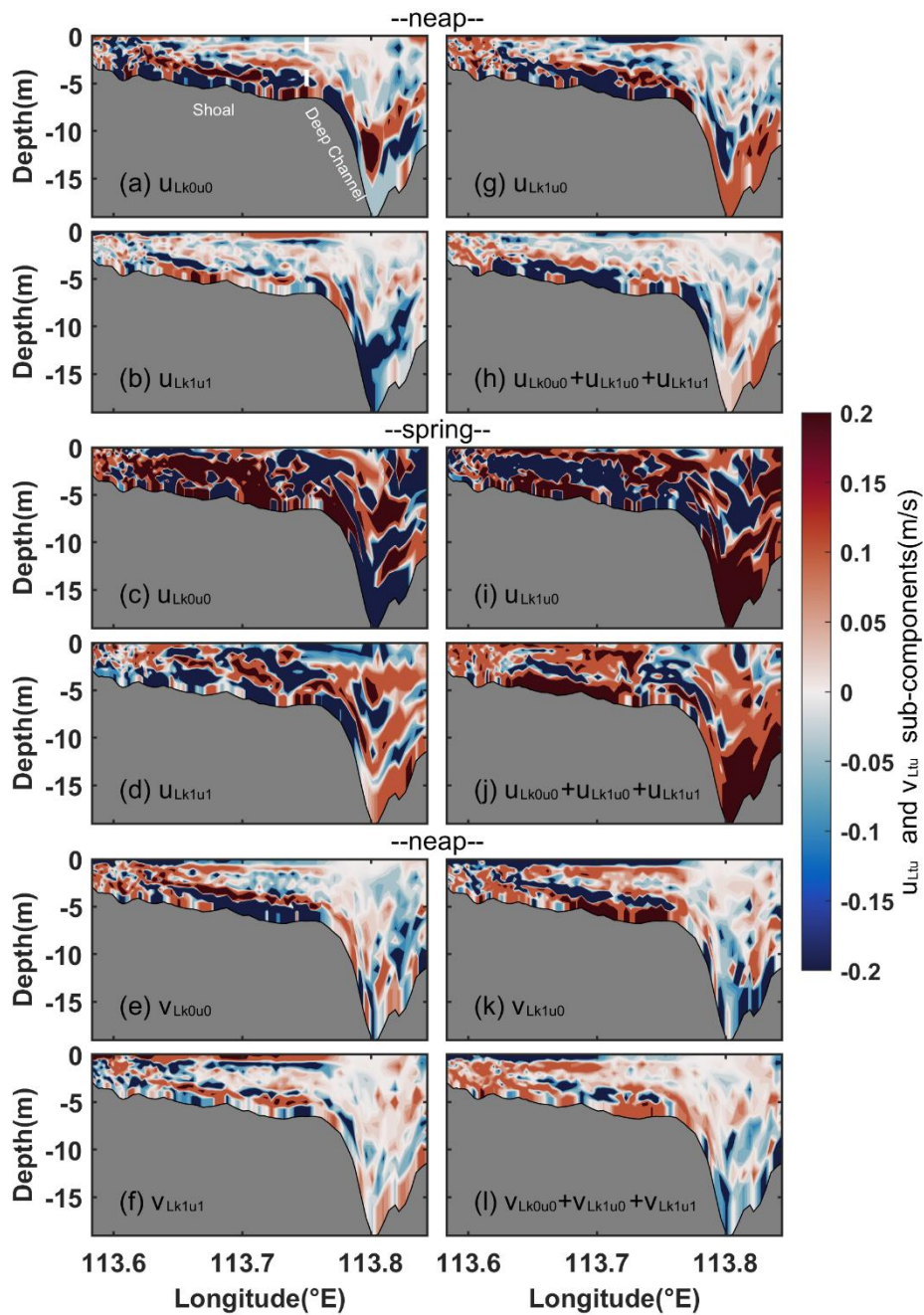
Figure 13 Vertical profiles of non-dominant subcomponents of cross-estuary (u_{Ltu}) and along-estuary (v_{Ltu}) eddy viscosity components for Case 1. For cross-estuary subcomponents: **(a, c)** coupled component of the tidal-average eddy viscosity and velocity gradient oscillation (u_{Lk0u0}), **(g, i)** tidal straining component (u_{Lk1u0}), **(b, d)** coupled component of eddy viscosity oscillation and the tidal-average velocity gradient (u_{Lk1u1}), **(h, j)** the sum of the three subcomponents during neap **(a, b, g, h)** and spring **(c, d, i, j)** tides, respectively. **(e, k, f, l)** Corresponding along-estuary eddy viscosity subcomponents during neap tides.

646   Without the wind forcing, the structures of the non-dominant components of the eddy

647   viscosity component in Case 2 remain consistent with those in Case 1 throughout the entire

648   cross section (not shown). However, during neap tides, their magnitudes in the upper layer

649   manifest a reduction by an order of magnitude relative to Case 1. This indicates a substantial

650   influence of wind on these subcomponents during relatively small tides. During spring tides,

651   both the structure and magnitude (Table 2) of each non-dominant component of the eddy

652   viscosity component align with those in Case 1. This suggests a weak influence of wind on the

653   non-dominant components during spring tides.

654   When stratification is further ignored in Case 3, the cross-estuary coupled component of

655   the tidal-averaged eddy viscosity and velocity gradient oscillation (u_{Lk0u0}) exhibits eastward

656   flow in the shoal and the lower layer of the deep channel, while displaying westward flow in

657   the upper layer of the deep channel during neap tides (Fig. 14a). This structure differs from that

658   in Case 2, and the magnitude of u_{Lk0u0} is approximately 140 times smaller than that in Case 2

659   (Table 2) during neap tides. The cross-estuary turbulent mean component (u_{Lk0u1}) for Case 3

660   predominantly flows westward in most of the shoal, and eastward in most of the deep channel

661   (Fig. 14b). The u_{Lk0u1} transitions from westward flow in Case 2 to eastward flow in Case 3 in

662   the lower layer of the deep channel. Furthermore, the magnitude of u_{Lk0u1} in Case 3 is

663   approximately 12 times smaller than that during neap tides in Case 2. During spring tides, the

664   area of eastward flow of u_{Lk0u0} in the shoal is larger than that observed during neap tides in

665   Case 3 (Fig. 14g), and its magnitude is approximately 6 times smaller than that in Case 2. The

666   structure of u_{Lk0u1} during spring tides aligns with that observed during neap tides (Fig. 14h),

667   while its magnitude is roughly 20 times smaller than that in Case 2. The magnitude of the cross-

668   estuary coupled component of eddy viscosity oscillation and tidal-average velocity gradient

669   (u_{Lk1u1}) (Fig. 14c and i) in Case 3 is the smallest among the components (Table 2),

670   approximately ranging from 40 to 50 times smaller than that in Case 2.

39

671   The along-estuary non-dominant eddy viscosity subcomponents for Case 3 are depicted

672   in Fig. 14d–f and j–l. During neap tides, both the along-estuary coupled component of the tidal-

673   averaged eddy viscosity and velocity gradient oscillation (v_{Lk0u0}) and the along-estuary coupled

674   component of eddy viscosity oscillation and tidal-average velocity gradient (v_{Lk1u1}) exhibit

675   horizontally sheared structures (Fig. 14d and f) that differ from those in Case 2. The magnitudes

676   of v_{Lk0u0} and v_{Lk1u1} are approximately 22–50 times smaller than those in Case 2 (Table 2).

677   During spring tides, the structures of v_{Lk0u0} and v_{Lk1u1} (Fig. 14j and l) are relatively similar to

678   those during neap tides, and their magnitudes are approximately 12–32 times smaller compared

679   to Case 2. During neap tides, the along-estuary turbulent mean component (v_{Lk0u1}) for Case 3

680   displays inflow in the shoal and the lower layer of the deep channel, as well as outflow in the

681   upper layer of the deep channel (Fig. 14e). This pattern is opposite to that in Case 2, and the

682   magnitude of v_{Lk0u1} is approximately 6 times smaller than that in Case 2. During spring tides,

683   the outflow area of v_{Lk0u1} for Case 3 in the deep channel is larger than that during neap tides

684   (Fig. 14k), and the magnitude is approximately 5 times smaller than that in Case 2. The results

685   elucidate the substantial effect of stratification on each non-dominant component of the eddy

686   viscosity due to the differentially sheared structure, with magnitudes an order greater than in

687   non-stratified scenarios.

Figure 14 Vertical profiles of non-dominant subcomponents of cross-estuary (u_{Ltu}) and along-estuary (v_{Ltu}) eddy viscosity components for Case 3. For cross-estuary subcomponents: **(a, g)** coupled component of the tidal-average eddy viscosity and velocity gradient oscillation (u_{Lk0u0}), **(b, h)** turbulent mean component (u_{Lk0u1}), **(c, i)** coupled component of eddy viscosity oscillation and the tidal-average velocity gradient (u_{Lk1u1}) during neap **(a–c)** and spring **(g–i)** tides, respectively. **(d, j, e, k, f, l)** Corresponding along-estuary eddy viscosity subcomponents.

41

4. Discussion

Several dimensionless parameters are examined to quantify the relative impact of the two distinct forcings, respectively. The Pearl River Estuary (PRE) features a relatively wide expanse, measuring 20–60 km in width in the middle and lower regions, away from the river discharge input nodes, and extending over a length of 70 km. The Rossby number is approximately 0.2 in the Pearl River Estuary (PRE), similar to that calculated by Li et al. (2023), signifying the prominence of the Coriolis force in the region's dynamics. The baroclinic Rossby deformation radius is estimated to be approximately 12–16 km, a range similar to the findings of Pan et al. (2014), suggesting the necessity to account for the rotational effect of the Earth. Lai et al. (2018) highlighted that the influence of the Coriolis force in the PRE is substantial with its effect extending to the bottom layer when compared to vertical mixing, and baroclinic and barotropic momentum when analyzing the Eulerian average momentum equation. Chen et al. (2019) indicated that in the depth-integrated momentum balance prior to a storm in the PRE, local momentum balance primarily involves the pressure gradient force, the Coriolis force, and bottom stress. Synthesizing current and prior research, it becomes apparent that the Coriolis force is a predominant factor influencing the dynamics of the PRE. This assertion is corroborated by Wu et al. (2018), who contend that the decomposition approach to Eulerian residual transport assumes particular significance in scenarios marked by a notable presence of Coriolis forces, as evidenced by a small Rossby number. The aforementioned discussion accentuates the criticality and practicality of employing decomposition methods in such analytical contexts.

The Pelect number (Pe), defined as $u_c L_c / v_{Dc}$, measures the relative contribution between the nonlinear advection and horizontal diffusion, where u_c, L_c, and v_{Dc} are the scales of tidal current, the estuary length, and the horizontal diffusion coefficient. The Pe for the PRE domain is several orders of magnitude larger than 1 indicating horizontal diffusion is so small that it

42

720   can be ignored. The results in the paper have indicated that the contribution of the horizontal

721   diffusion component is several-fold lower, or even an order of magnitude, less than other

722   components. Among all terms, the barotropic pressure gradient has the largest scale, making

723   the barotropic pressure gradient component of LRV contribute the most compared to other

724   components. The Wedderburn number (W) is calculated to measure the contribution ratio of

725   wind forcing to the baroclinic pressure gradient, defined as $W = L_c T_w / (g \triangle \rho H_c^2)$ (Lange and

726   Burchard, 2019). The value of W in the PRE is 0.0294 during neap tides and 0.0447 during

727   spring tides, suggesting the baroclinic effects dominate in periodically stratified waters and

728   small W inhibits along-estuary gravitational circulation, which is identical to that in Lange and

729   Burchard (2019). The Simpson number (Si) is a parameter used to quantify the level of

730   stratification in estuaries (Simpson et al., 1990). It is calculated using the following formula:

$$Si = \frac{\partial_x b H^2}{u_{max}^2},\tag{8}$$

731   where $\partial_x b$ represents the tidal mean horizontal density gradient, H represents the water depth,

732   and u_{max} represents the absolute magnitude of the velocity amplitude. Based on the Simpson

733   number values, different stratification conditions can be determined for the estuary. The estuary

734   is categorized as well-mixed when $Si < 0.088$; In the case of $0.088 < Si < 0.84$, the estuary

735   displays periodic stratification; For $Si > 0.84$, the estuary is strongly stratified, as indicated by

736   Becherer et al. (2011). The Si for the PRE ranges from 0.1 to 0.45 in stratified conditions in

737   Cases 1 and 2, indicating that the estuary is periodically stratified. Sections B–D are arranged

738   in a north-to-south distribution, gradually approaching the open sea. The Si progressively

739   increases towards the open sea, with values ranging from 0.1 to 0.4 during neap tides and 0.05

740   to 0.1 during spring tides. This indicates that the magnitude of tides has substantial influences

741   on Si. With the increment in Si, the relative contributions of the tidal straining component and

742   the baroclinic pressure gradient component diminish. These findings align with those of Cheng

743   et al. (2011). Forced by wind, the relative contribution of the two components changes from 2

744   to 0.57 during neap tides and 2 to 1.4 during spring tides. However, in the absence of wind, the

745   relative contribution varies from 0.67 to 0.26 during neap tides and 1.4 to 0.9 during spring

746   tides, where the value of Si closely mirrors those with wind forcing. The findings underscore

747   that the southwesterly wind amplifies the relative contribution ratios of the tidal straining

748   component to the baroclinic pressure gradient component of the LRV. Specifically, these ratios

749   are 1.5 to 3 times greater compared to scenarios without wind forcing.

750   According to the Eulerian mean theory, the coupled component of tidal-averaged eddy

751   viscosity and velocity gradient oscillation (u_{Ek0u0}), and the coupled component of tidal-

752   averaged velocity gradient and eddy viscosity oscillation (u_{Ek1u1}) are zero (Burchard and

753   Hetland, 2010), however, in the Lagrangian mean theory, those components are not zero and

754   their magnitudes are comparable to other components under most conditions. Although the

755   tidal straining component of ERV has been extensively discussed, the contribution of the

756   turbulent mean term to the total ERV has not been analyzed in previous studies (Burchard and

757   Hetland, 2010; Burchard et al., 2011). This paper reveals that under stratified conditions, the

758   tidal mean component dominates the eddy viscosity component, even though the magnitudes

759   of tidal straining and the combined component of tidal-average eddy viscosity and velocity

760   gradient oscillation are greater than the turbulent mean component. However, these two

761   components exhibit inverse structures of equal magnitude. As a result, their collective impact

762   on the total eddy viscosity component is minimal or negative. Under homogeneous conditions,

763   the tidal straining component dictates the structure of the eddy viscosity. Similarly, the

764   cumulative effects of other components contribute negatively and minimally.

765   The decomposition methodologies present distinct advantages for elucidating the

766   dynamics of Lagrangian Residual Velocity (LRV) within generally or weakly nonlinear

767   systems. This significance stems from the absence of comprehensive analytical solutions and

768   definitive governing equations for LRV in generally nonlinear contexts, coupled with the

769   constraints of analytical solutions in weakly nonlinear frameworks (Jiang and Feng, 2014; Cui

770   et al., 2019; Chen et al., 2020). In scenarios where the Coriolis force is negligible, the

771   Lagrangian mean momentum equations remain applicable for primary momentum balance

772   analysis. However, these equations are inadequate for the detailed dissection of each LRV

773   component. Notably, in circumstances where the Coriolis effect is minimally impactful, the

774   methodologies employed for LRV decomposition may demonstrate variability, contingent

775   upon the dominant momentum balances. This underscores the necessity for expanded

776   investigation in future scholarly endeavors.

777   The relevance of the Lagrangian residual circulation for mass transport in estuaries or

778   bays is evident. In the Eulerian-averaged salinity balance equation, a tidal dispersion term

779   emerges (Hansen and Rattray, 1965). This tidal dispersion term exhibits different dynamic

780   mechanisms in various estuaries (Fischer, 1979), and even within different sections of the same

781   estuary. However, when the isohaline averaging method is employed to quantitatively assess

782   estuarine circulation, the tidal dispersion term vanishes (MacCready, 2011; Wang et al., 2017;

783   MacCready et al., 2018). Nevertheless, the salinity coordinate method is only an approximate

784   Lagrangian approach. Future studies focusing on the dynamic mechanisms of salinity transport

785   from a Lagrangian averaging perspective will provide further insights into the subject.

786   **5. Conclusions**

787   The FVCOM model is employed to investigate the dynamic mechanism of the LRV in the

788   PRE. By quantitatively analyzing the contribution of each dynamic component to the LRV, the

789   primary mechanisms governing the LRV in the PRE under conditions of stratification and wind

790   are elucidated, which has been not extensively explored in prior studies (Chu et al., 2022; Deng

791   et al., 2022). Moreover, to discern the impact of the eddy viscosity component on the LRV,

792 this component is decomposed into four subcomponents, with each subcomponent's

793 contribution being quantitatively evaluated. Notably, the decomposition methodologies rooted

794 in Lagrangian theory adopted in this work differ from earlier studies anchored in Eulerian

795 theory (e.g., Burchard et al., 2011; Cheng et al., 2011; Wei et al., 2021). This analysis reveals

796 the prevailing mechanisms shaping the structure of the eddy viscosity component across

797 different dynamic scenarios.

798   While many studies have focused on ERV in the PRE (e.g., Lai et al., 2018; Xu et al.,

799 2021; Hong et al., 2022), research on LRV in the PRE remains limited, particularly regarding

800 the dynamic mechanisms of LRV. In the reference case, the cross-estuary LRV (u_L) exhibits a

801 two-layer vertical structure with eastward flow in the upper layer and westward flow in the

802 lower layer. The two-layer structure is primarily determined by the combined effects of the

803 eddy viscosity component (u_{Ltu}), the barotropic pressure gradient component (u_{Lba}), and the

804 baroclinic pressure gradient component (u_{Lgr}). The u_{Ltu} is the main contributor to the eastward

805 flow in the upper layer of the shoal, and u_{Lba} determines the eastward flow in the upper layer

806 of the deep channel. For the entire lower layer, the westward flow is dominated by u_{Ltu} and u_{Lba},

807 with u_{Lgr} playing a balancing role. The along-estuary LRV (v_L) exhibits a two-layer

808 gravitational circulation pattern. The v_L is predominantly influenced by the imbalance of the

809 barotropic pressure gradient component (v_{Lba}) and the baroclinic pressure gradient component

810 (v_{Lgr}). The outflow is mainly dominated by v_{Lba} in the upper layer, while the inflow is primarily

811 driven by v_{Lgr} in the lower layer. For non-dominant components, the combined effects of the

812 local acceleration component, and the horizontal and vertical nonlinear component contributes

813 less to total LRV. The contribution of the horizontal diffusion component is negligible.

814   Without wind forcing, the eastward flow dominated by the eddy viscosity component (u_{Ltu})

815 transforms into the westward flow dominated by the barotropic pressure gradient component

816 (u_{Lba}) in the upper 2 m of the shoal. In other regions, the dominant components of the cross-

817 estuary LRV (u_L) roughly remain the same as those in the reference case, indicating that wind

818 mainly affects u_L in the upper layer by influencing u_{Ltu}. The structure and dominant components

819 of the along-estuary LRV (v_L) are nearly consistent with those in the reference case except for

820 some regions in the shoal, but the magnitude of the dominant components is larger than that in

821 the reference case, indicating that the southwesterly wind inhibits the along-estuary

822 gravitational circulation. The along-estuary non-dominant components exhibit consistent

823 magnitudes and structures, irrespective of the presence or absence of wind forcing, except for

824 the along-estuary eddy viscosity component, which exhibits a reverse structure in the upper

825 layer compared to that with wind forcing.

826   Under unstratified conditions, the cross-estuary and along-estuary LRV (u_L, v_L) are

827 transformed from the vertical shear structure in stratified waters to the lateral shear structure.

828 The u_L is dominated by the sum of the local acceleration component (u_{Lac}), horizontal nonlinear

829 component (u_{Ladh}), barotropic pressure gradient component (u_{Lba}), and eddy viscosity

830 component (u_{Ltu}). The v_L is dominated by the sum of the barotropic pressure gradient

831 component (v_{Lba}) and eddy viscosity component (v_{Ltu}). These results indicate that stratification

832 modulates the structure of the LRV by impacting its dominant components when contrasted

833 with conditions in homogeneous waters.

834   This study highlights that the eddy viscosity component remains dominant regardless of

835 the presence of stratification. Specifically, under stratified conditions, the turbulent mean

836 component plays a dominant role in the total eddy viscosity component, which has not yet been

837 studied in previous works (e.g., Burchard et al., 2023). Conversely, under unstratified

838 conditions, the tidal straining component takes precedence over other factors in contribution to

839 the total eddy viscosity component, and its magnitude is either several times or one order of

840 magnitude bigger than the other components. The combined effects of non-dominant

841 components have a negative contribution to the total eddy viscosity component.

Appendix

Numerical solutions of each component of the Lagrangian Residual Velocity (LRV)

Each term in the momentum equations is integrated along the particle trajectories over a tidal period and divided by the tidal period to obtain each dynamic component of Lagrangian residual velocity.

$$v_L = \underbrace{\langle\frac{\partial uD}{D\partial t}\rangle/f}_{1} + \underbrace{\langle\frac{\partial u^2 D}{D\partial x} + \frac{\partial uvD}{D\partial y}\rangle/f}_{2} + \underbrace{\langle\frac{\partial u\omega D}{D\partial \sigma}\rangle/f}_{3} + \underbrace{\langle g\frac{\partial \zeta}{\partial x}\rangle/f}_{4}$$

$$\underbrace{-\langle\frac{1}{D^2}\frac{\partial}{\partial \sigma}\left(v_h\frac{\partial u}{\partial \sigma}\right)\rangle/f}_{5} + \underbrace{\langle\frac{g}{\rho_0}\left(D\int_\sigma^0 \frac{\partial \rho}{\partial x}d\sigma_1 + \frac{\partial D}{\partial x}\int_\sigma^0 \sigma_1\frac{\partial \rho}{\partial \sigma_1}d\sigma_1\right)\rangle/f}_{6} \underbrace{-\langle F_x\rangle/f}_{7}, \quad (A1)$$

$$u_L = \underbrace{-\langle\frac{\partial vD}{D\partial t}\rangle/f}_{1} - \underbrace{\langle(\frac{\partial uvD}{D\partial x} + \frac{\partial v^2 D}{D\partial y})\rangle/f}_{2} - \underbrace{\langle\frac{\partial v\omega D}{D\partial \sigma}\rangle/f}_{3} - \underbrace{\langle g\frac{\partial \zeta}{\partial y}\rangle/f}_{4}$$

$$+ \underbrace{\langle\frac{1}{D^2}\frac{\partial}{\partial \sigma}\left(v_h\frac{\partial v}{\partial \sigma}\right)\rangle/f}_{5} - \underbrace{\langle\frac{g}{\rho_0}\left(D\int_\sigma^0 \frac{\partial \rho}{\partial y}d\sigma_1 + \frac{\partial D}{\partial y}\int_\sigma^0 \sigma_1\frac{\partial \rho}{\partial \sigma_1}d\sigma_1\right)\rangle/f}_{6} + \underbrace{\langle F_y\rangle/f}_{7}, \quad (A2)$$

where u (x, y, σ, t), v (x, y, σ, t), and ω (x, y, σ, t) represent velocity components in the longitudinal (x), latitudinal (y), and vertical (σ) directions, respectively. The ρ (x, y, σ, t) is water density, ρ_0 is the reference density, t is the time, f is the Coriolis parameter, and v_h (x, y, σ, t) is eddy viscosity coefficient. The $D = H + \zeta$, where H (x, y) is the water mean depth, $\zeta(x, y, t)$ is the water surface elevation. The first term refers to local acceleration component, the second terms represent horizontal nonlinear advection components, the third term depicts the nonlinear vertical advection component, the fourth term corresponds to the barotropic pressure gradient component, the fifth term describes the eddy viscosity component, the sixth terms denote the baroclinic pressure gradient components, and the seventh term pertains to horizontal diffusion component. The $<>$ denotes the Lagrangian mean operator.

Data availability

Hydrodynamic datasets used in this study are available online at

859 https://doi.org/10.5281/zenodo.10043226 (Deng et al., 2023). The 1° World Ocean Atlas 2009

860 (WOA2009) datasets are accessible online from (https://accession.nodc.noaa.gov/0094866).

861 The 0.25° CCMP datasets are available online (http://www.remss.com/measurements/ccmp).

862 The monthly average river runoff data are provided by the Water Conservancy Committee of

863 the Pearl River under the Ministry of Water Resources. The topography data off the PRE are

864 from the ETOPO2 dataset of NOAA

865 (https://www.ngdc.noaa.gov/mgg/global/relief/ETOPO2/ETOPO2v2-2006/), while those

866 within the estuary are provided by the China Maritime Safety Administration.

867 **Author contributions**

868 All authors have contributed to the conceptualization and design of this study. The

869 analytical methods were originally formulated by FD. Subsequently, FD and ZC meticulously

870 processed and analyzed the data. The model was collaboratively developed and the manuscript

871 was co-authored by FD, FJ, and ZC. The final manuscript underwent a thorough review and

872 editing process, led by RS, SZ, QL, and XZ, ensuring its quality and accuracy.

873 **Competing interests**

874 The contact author has declared that none of the authors has any competing interests.

881 **References**

882 Abbott, M. R.: Boundary layer effects in estuaries, J. Mar. Res., 18, 83–100, 1960.

883   Becherer, J., Burchard, H., Flöser, G., Mohrholz, V., Umlauf, L.: Evidence of tidal straining in well-mixed
884   channel flow from micro-structure observations, Geophys. Res. Lett., 38(17),
885   https://doi.org/10.1029/2011GL049005, 2011.

886   Burchard, H.: Combined effects of wind, tide and horizontal density gradients on stratification in estuaries
887   and coastal seas, J. Phys. Oceanogr., 39, 2117–2136, https://doi.org/10.1175/2009JPO4142.1, 2009.

888   Burchard, H., Bolding, K., Lange, X., Osadchiev, A.: Decomposition of Estuarine Circulation and Residual
889   Stratification under Landfast Sea Ice, J. Phys. Oceanogr., 2023, 53(1), 57–80, 2023.

890   Burchard, H., Hetland, R. D.: Quantifying the contributions of tidal straining and gravitational circulation to
891   residual circulation in periodically stratified tidal estuaries, J. Phys. Oceanogr., 40(6), 1243–1262,
892   https://doi.org/10.1175/2010JPO4270.1, 2010.

893   Burchard, H., Hetland, R. D., Schulz, E., Schuttelaars, H. M.: Drivers of residual estuarine circulation in
894   tidally energetic estuaries: Straight and irrotational channels with parabolic cross section, J. Phys.
895   Oceanogr., 41(3), 548–570, https://doi.org/10.1175/2010JPO4453.1, 2011.

896   Burchard, H., Schulz, E., Schuttelaars, H. M.: Impact of estuarine convergence on residual circulation in
897   tidally energetic estuaries and inlets, Geophys. Res. Lett., 41(3), 913–919, https://doi.
898   org/10.1002/2013GL058494, 2014.

899   Chen, C. S., Beardsley, R. C., Cowles, G.: An unstructured grid, finite volume coastal ocean model (FVCOM)
900   system, Oceanography, 19, 78–89, https://doi.org/10.5670/oceanog.2006.92, 2006.

901   Chen, C. S., Liu, H. D., Beardsley, R. C.: An unstructured grid, finite-volume, three-dimensional, primitive
902   equations ocean model: application to coastal ocean and estuaries, J. Atmos. Ocean. Tech., 20(1), 159–
903   186, 2003.

904   Chen, S. M.: Water Exchange Due to Wind and Waves in a Monsoon Prevailing Tropical Atoll, J. Mar. Sci.
905   Eng., 11(1), 109, 2023.

906   Chen, Y., Cui, Y. X., Sheng, X. X., Jiang, W. S., Feng, S. Z.: Analytical solution to the 3D tide-induced
907   Lagrangian residual current in a narrow bay with vertically varying eddy viscosity coefficient, Ocean
908   Dyn., 70, 759–770, https://doi.org/10.1007/s10236-020-01359-3, 2020.

909 Chen, Y. R., Chen, L. H., Zhang, H., Gong, W. P.: Effects of wave-current interaction on the Pearl River

910   Estuary during Typhoon Hato, Estuar. Coast. Shelf Sci., 228, 106364,

911   https://doi.org/10.1016/j.ecss.2019.106364, 2019.

912 Cheng, P.: Decomposition of residual circulation in estuaries, J. Atmos. Ocean. Tech., 31(3), 698–713, 2014.

913 Cheng, P., Valle-Levinson, A., de Swart, H. E.: A numerical study of residual circulation induced by

914   asymmetric tidal mixing in tidally dominated estuaries, J. Geophys. Res.: Oceans, 116(C1),

915   https://doi.org/10.1029/2010JC006137, 2011.

916 Chu, N. Y., Liu, G. L., Xu, J., Yao, P., Du, Y., Liu, Z. Q., Cai, Z. Y.: Hydrodynamical transport structure and

917   lagrangian connectivity of circulations in the Pearl River Estuary, Front. Mar. Sci., 9, 996551,

918   https://doi.org/10.3389/fmars.2022.996551, 2022.

919 Cui, Y. X., Jiang, W. S., Deng, F. J.: 3D numerical computation of the tidally induced Lagrangian residual

920   current in an idealized bay, Ocean Dyn., 69, 283–300, https://doi.org/10.1007/s10236-018-01243-1,

921   2019.

922 Deng, F. J., Jiang, W. S., Feng, S. Z.: The nonlinear effects of the eddy viscosity and the bottom friction on

923   the Lagrangian residual velocity in a narrow model bay, Ocean Dyn., 67, 1105–1118,

924   https://doi.org/10.1007/s10236-017-1076-x, 2017.

925 Deng, F. J., Jiang, W. S., Valle-Levinson, A., Feng, S. Z.: 3D modal solution for tidally induced Lagrangian

926   residual velocity with variations in eddy viscosity and bathymetry in a narrow model bay, J. Ocean Univ.

927   China, 18, 69–79, https://doi.org/10.1007/s11802-019-3773-1, 2019.

928 Deng, F. J., Jiang, W. S., Zong, X. L., Chen, Z. Y.: Quantifying the Contribution of Each Driving Force to

929   the Lagrangian Residual Velocity in Xiangshan Bay, Front. Mar. Sci., 9, 901490,

930   https://doi.org/10.3389/fmars.2022.901490, 2022.

931 Egbert, G. D., Erofeeva, S. Y.: Efficient inverse modeling of barotropic ocean tides, J. Atmos. Ocean. Tech.,

932   19(2), 183–204, 2002.

933 Feng, S. Z.: A three-dimensional weakly nonlinear model of tide-induced Lagrangian residual current and
934　　mass-transport, with an application to the Bohai Sea, Elsevier Oceanogr. Ser., 45, 471–488,
935　　https://doi.org/10.1016/S0422-9894(08)70463-X, 1987.

936 Feng, S. Z., Xi, P. G., Zhang, S. Z.: The baroclinic residual circulation in shallow seas: I. The hydrodynamic
937　　models, Chin. J. Oceanol. Limnol., 2, 49–60, https://doi.org/10.1007/BF02888391, 1984.

938 Fischer, H. B., List, J., Koh, C. R., Imberger, J., Brooks, N. H.: Mixing in inland and coastal waters,
939　　Academic Press, https://doi.org/10.1016/C2009-0-22051-4, 1979.

940 Geyer, W. R., MacCready, P.: The estuarine circulation, Annu. Rev. Fluid Mech., 46, 175–197,
941　　https://doi.org/10.1146/annurev-fluid-010313-141302, 2014.

942 Geyer, W. R., Ralston, D. K., Chen, J. L.: Mechanisms of exchange flow in an estuary with a narrow, deep
943　　channel and wide, shallow shoals, J. Geophys. Res.: Oceans, 125, e2020JC016092, https://
944　　doi.org/10.1029/2020-JC016092, 2020.

945 Gong, W. P., Lin, Z. Y., Chen, Y. Z., Chen, Z. Y., Zhang, H.: Effect of winds and waves on salt intrusion in
946　　the Pearl River estuary, Ocean Sci., 14(1), 139–159, https://doi.org/10.5194/os-14-139-2018, 2018.

947 Hansen, D. V., Rattray, M.: Gravitational circulation in straits and estuaries, J. Mar. Res., 79(2), 69–87,
948　　https://doi.org/10.1357/002224021834614399, 1965.

949 Hewageegana, V. H., Olabarrieta, M., Gonzalez-Ondina, J. M.: Main Physical Processes Affecting the
950　　Residence Times of a Micro-Tidal Estuary, J. Mar. Sci. Eng., 11(7), 1333, 2023.

951 Hong, B., Xue, H. L., Zhu, L. S., Xu, H. Z.: Climatic Change of Summer Wind Direction and Its Impact on
952　　Hydrodynamic Circulation in the Pearl River Estuary, J. Mar. Sci. Eng., 10, 10070842,
953　　https://doi.org/10.3390/jmse10070842, 2022.

954 Ianniello, J. P.: Tidally induced residual currents in estuaries of constant breadth and depth, J. Mar. Res., 9(5),
955　　962–974, 1977.

956 Jay, D. A., Musiak, J. D.: Particle trapping in estuarine tidal flows, J. Geophys. Res.: Oceans, 99(C10),
957　　20445–20461, https://doi.org/10.1029/94JC00971, 1994.

958 Jiang, M. S.: Modeling Water Residence Time and Connectivity in the Northern Indian River Lagoon,

959   Estuaries Coasts, 1–20, 2023.

960 Jiang, W. S., Feng, S. Z.: Analytical solution for the tidally induced Lagrangian residual current in a narrow

961   bay, Ocean Dyn., 61, 543–558, https://doi.org/10.1007/s10236-011-0381-z, 2011.

962 Jiang, W. S., Feng, S. Z.: 3D analytical solution to the tidally induced Lagrangian residual current equations

963   in a narrow bay, Ocean Dyn., 64, 1073–1091, https://doi.org/10.1007/s10236-014-0738-1, 2014.

964 Jongbloed, H., Schuttelaars, H. M., Dijkstra, Y. M., Donkers, P. B., Hoitink, A. J.: Influence of wind on

965   subtidal salt intrusion and stratification in well-mixed and partially stratified estuaries, J. Phys.

966   Oceanogr., 52(12), 3139–3158, https://doi.org/10.1175/JPO-D-21-0291.1, 2022.

967 Kukulka, T., Chant, R. J.: Surface convergence zones due to Lagrangian residual flow in tidally driven

968   estuaries, J. Phys. Oceanogr., 53(2), 423–431, 2023.

969 Lai, W. F., Pan, J. Y., Devlin, A. T.: Impact of tides and winds on estuarine circulation in the Pearl River

970   Estuary, Cont. Shelf Res., 168, 68–82, https://doi.org/10.1016/j.csr.2018.09.004, 2018.

971 Lamb, H.: Hydrodynamics, London: Cambridge university press, 1975.

972 Lange, X., Burchard, H.: The relative importance of wind straining and gravitational forcing in driving

973   exchange flows in tidally energetic estuaries, J. Phys. Oceanogr., 49(3), 723–736,

974   https://doi.org/10.1175/JPO-D-18-0014.1, 2019.

975 Levitus, S., Antonov, J. I., Baranova, O. K., Boyer, T. P., Coleman, C. L., Garcia, H. E., Grodsky, A. I.,

976   Johnson, D. R., Locarnini, R. A., Mishonov, A. V., Reagan, J. R., Sazama, C. L., Seidov, D., Smolyar, I.,

977   Yarosh, E. S., Zweng, M. M.: The world ocean database. Data Science Journal, 12, WDS229-WDS234,

978   2013.

979 Li, M. Q., Wang, N., Li, G. X., Song, D. H., Gu, Y. Z., Bao, X. W., Liu, S. D., Zhang, L.: Plume bulge

980   observed in the Pearl River Estuary in summer: Spatiotemporal characteristics and influencing factors,

981   Estuar. Coast. Shelf Sci., 282, 108242, 2023.

982 Li, S. Z., Zhang, Z. R., Zhou, M., Wang, C. N., Wu, H., Zhong, Y. S.: The role of fronts in horizontal

983   transports of the Changjiang River plume in summer and the implications for phytoplankton blooms, J.

984   Geophys. Res.: Oceans, 127(8), e2022JC018541 2022.

985 Lin, L., Liu, D. Y., Fu, Q. J., Guo, X. Y., Liu, G. L., Liu, H., Wang, S. L.: Seasonal variability of water

986   residence time in the Subei Coastal Water, Yellow Sea: The joint role of tide and wind, Ocean Model.,

987   180, 102137, https://doi.org/10.1016/j.ocemod.2022.102137, 2022.

988 Liu, G. L., Liu, Z., Gao, H. W., Feng, S. Z.: Initial time dependence of wind- and density-driven Lagrangian

989   residual velocity in a tide-dominated bay, Ocean Dyn., 71, 447–469, https://doi.org/10.1007/s10236-

990   021-01447-y, 2021.

991 MacCready, P.: Calculating estuarine exchange flow using isohaline coordinates, J. Phys. Oceanogr., 41,

992   1116–1124, https://doi.org/10.1175/2011JPO4517.1, 2011.

993 MacCready, P., Geyer, W. R., Burchard, H.: Estuarine exchange flow is related to mixing through the salinity

994   variance budget, J. Phys. Oceanogr., 48, 1375–1384, https://doi.org/10.1175/JPO-D-17-0266.1, 2018.

995 Mears, C., Lee, T., Ricciardulli, L., Wang, X. C., Wentz, F.: Rss cross-calibrated multi-platform (Ccmp) 6-

996   hourly ocean vector wind analysis on 0.25 deg grid, version 3.0, Remote Sens., Syst, 2022.

997 NOAA National Geophysical Data Center.: 2-minute Gridded Global Relief Data (ETOPO2) v2. NOAA

998   National Centers for Environmental Information, https://doi.org/10.7289/V5J1012Q, 2006.

999 Pan, J. Y., Gu, Y. Z.: Cruise observation and numerical modeling of turbulent mixing in the Pearl River

1000   estuary in summer, Cont. Shelf Res., 120, 122–138, 2016.

1001 Pan, J. Y., Gu, Y. Z., Wang, D. X.: Observations and numerical modeling of the Pearl River plume in summer

1002   season, J. Geophys. Res.: Oceans, 119, 2480–2500, https://doi.org/10.1002/2013JC009042, 2014.

1003 Pan, J. Y., Lai, W. F., Devlin, A. T.: Channel-Trapped Convergence and Divergence of Lateral Velocity in

1004   the Pearl River Estuary: Influence of Along-Estuary Variations of Channel Depth and Width, J. Geophys.

1005   Res.: Oceans, 125(1), e2019JC015369, https://doi.org/10.1029/2019JC015369, 2020.

1006 Pritchard, D. W.: Estuarine hydrography, Adv. Geophys., 1, 243–280, https://doi.org/10.1016/S0065-

1007   2687(08)60208-3, 1952.

1008   Pritchard, D. W.: The dynamic structure of a coastal plain estuary, J. Mar. Res., 15(1), 33–42, 1956.

1009   Quan, Q., Mao, X. Y., Jiang, W. S.: Numerical computation of the tidally induced Lagrangian residual current
1010   in a model bay, Ocean Dyn., 64, 471–486, https://doi.org/10.1007/s10236-014-0696-7, 2014.

1011   Ren, L., Yang, L. N., Pan, G. W., Zheng, G., Zhu, Q., Wang, Y. Q., Zhu, Z. C., Hartnett, M.: Characterizing
1012   Residual Current Circulation and Its Response Mechanism to Wind at a Seasonal Scale Based on High-
1013   Frequency Radar Data, Remote Sens., 14, 14184510, https://doi.org/10.3390/rs14184510, 2022.

1014   Sheng, X. X., Mao, X. Y., Yu, J. Z., Zhang, X. Q., Jiang, W. S., Lu, Y. Y.: Modeling Lagrangian residual
1015   velocity in a tide-dominated long-narrow bay: case study of the inner Xiangshan Bay, Estuar. Coast.
1016   Shelf Sci., 278, 108088, https://doi.org/10.1016/j.ecss.2022.108088, 2022.

1017   Simpson, J. H., Brown, J., Matthews, J., Allen, G.: Tidal straining, density currents, and stirring in the control
1018   of estuarine stratification, Estuaries 13, 125–132, https://doi.org/10.2307/1351581, 1990.

1019   Soto-Riquelme, C., Pinilla, E., Ross, L.: Wind influence on residual circulation in Patagonian channels and
1020   fjords, Cont. Shelf Res., 254, 104905, 2023.

1021   Verspecht, F., Rippeth, T. P., Howarth, M. J., Souza, A. J., Simpson, J. H., Burchard, H.: Processes impacting
1022   on stratification in a region of freshwater influence: Application to Liverpool Bay, J. Geophys. Res.:
1023   Oceans, 114(C11), https://doi.org/10.1029/2009JC005475, 2009.

1024   Wang, B.: Analysis on the estuarine circulation and its dynamic mechanism in the Lingdingyang Bay,
1025   Chinese Journal of Hydrodynamics, 29(05), 608–617, 2014.

1026   Wang, J. H., Shen, Y. M., Guo, Y. K.: Seasonal circulation and influence factors of the Bohai Sea: a numerical
1027   study based on Lagrangian particle tracking method, Ocean Dyn., 60, 1581–1596,
1028   https://doi.org/10.1007/s10236-010-0346-7, 2010.

1029   Wang, T., Geyer, W. R., MacCready, P.: Total exchange flow, entrainment, and diffusive salt flux in estuaries,
1030   J. Phys. Oceanogr., 47, 1205–1220, https://doi.org/10.1175/JPO-D-16-0258.1, 2017.

1031   Wei, X. Y., Schuttelaars, H. M., Williams, M. E., Brown, J. M., Thorne, P. D., Amoudry, L. O.: Unraveling
1032   interactions between asymmetric tidal turbulence, residual circulation, and salinity dynamics in short,

1033   periodically   weakly   stratified   estuaries,   J.   Phys.   Oceanogr.,   51(5),   1395–1416,

1034   https://doi.org/10.1175/JPO-D-20-0146.1, 2021.

1035   Wei, X. Y., Williams, M. E., Brown, J. M., Thorne, P. D., Amoudry, L. O.: Salt intrusion as a function of

1036   estuary length in periodically weakly stratified estuaries, Geophys. Res. Lett., 49(15), e2022GL099082,

1037   https://doi.org/10.1029/2022GL099082, 2022.

1038   Willmott,   C.   J.,:   On   the   validation   of   models,   Phys.   Geogr.,   2,   184–194,

1039   https://doi.org/10.1080/02723646.1981.10642213, 1981.

1040   Winant, C. D.: Three-dimensional residual tidal circulation in an elongated, rotating basin, J. Phys. Oceanogr.,

1041   38(6), 1278–1295, https://doi.org/10.1175/2007JPO3819.1, 2008.

1042   Wu, H., Gu, J. H., Zhu, P.: Winter counter-wind transport in the inner southwestern Yellow Sea, J. Geophys.

1043   Res.: Oceans, 123(1), 411–436, 2018.

1044   Xu, H. Z., Shen, J., Wang, D. X., Luo, L., Hong, B.: Nonlinearity of subtidal estuarine circulation in the

1045   Pearl River Estuary, China, Front. Mar. Sci., 8, 629403, https://doi.org/10.3389/fmars.2021.629403,

1046   2021.

1047   Xue, H. J., Chai, F., Wang, L. Y., Chen, J. Z.: Zhujiang River Estuarine circulation model, China Ocean Press,

1048   147–160, 2001.

1049   Young, J. S., Hoon, Y. K., Jongseong, R., Kyung, H. H.: Wind-induced switch of estuarine residual

1050   circulations and sediment transport in micro-tidal bay, Estuar. Coast. Shelf Sci., 288, 2023.

1051   Yu, J. Z., Zhang, X. Q., Sheng, X. X., Jiang, W. S.: Mass transport pattern and mechanism in the tide-

1052   dominant Bohai Sea, Ocean Model., 182, 2023.

1053   Zhang, D. Q., Pang, C. G., Liu, Z. L., Jiang, J. B.: Winter and summer sedimentary dynamic process

1054   observations in the sea area off Qinhuangdao in the Bohai Sea, China, Front. Earth Sci., 11, 1097033,

1055   https://doi.org/10.3389/feart.2023.1097033, 2023.

1056   Zimmerman, J. T. F.: On the Euler-Lagrange transformation and the Stokes' drift in the presence of

1057   oscillatory and residual currents, Deep-Sea Res., 26A, 505–520, 1979.